Green Chemistry

Cutting-edge research for a greener sustainable future

Accepted Manuscript

Published on 03 November 2026
Licence and permissions

Check for updates

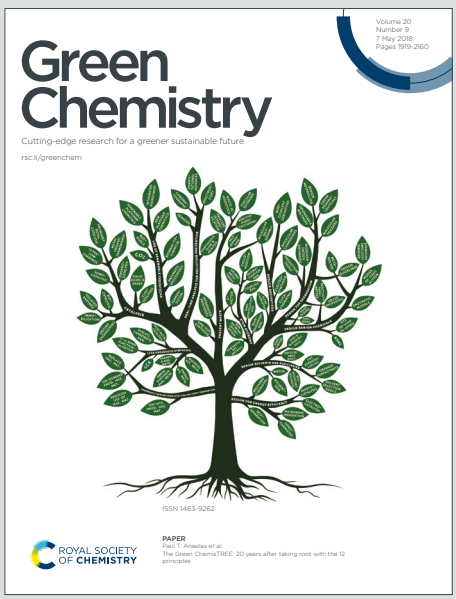

This is an Accepted Manuscript, which has been through the Royal Society of Chemistry peer review process and has been accepted for publication.

Accepted Manuscripts are published online shortly after acceptance, before technical editing, formatting and proof reading. Using this free service, authors can make their results available to the community, in citable form, before we publish the edited article. We will replace this Accepted Manuscript with the edited and formatted Advance Article as soon as it is available.

You can find more information about Accepted Manuscripts in the Information for Authors.

Please note that technical editing may introduce minor changes to the text and/or graphics, which may alter content. The journal's standard Terms & Conditions and the Ethical guidelines still apply. In no event shall the Royal Society of Chemistry be held responsible for any errors or omissions in this Accepted Manuscript or any consequences arising from the use of any information it contains.

Green Foundation Box

1. This review highlights single-atom photocatalysis as a sustainable platform for organic synthesis. By maximizing metal atom utilization and enabling light-driven reactions under mild conditions, SAC-based systems significantly reduce metal waste, energy consumption, and reliance on stoichiometric reagents compared with traditional catalytic redox approaches.

2. Photocatalytic organic transformations mediated by SACs align closely with several principles of green chemistry, including atom economy, energy efficiency, minimized waste, and catalyst recyclability. The heterogeneous nature of SACs facilitates catalyst recovery and reuse while avoiding issues associated with homogeneous metal complexes.

3. The mechanistic insights and catalyst-design strategies summarized in this review, such as coordination environment engineering, defect regulation, and cooperative multi-site catalysis provide guidance for developing next-generation photocatalytic systems, accelerating the transition toward greener and more sustainable chemical synthesis.

Green Chemistry Accepted Manuscript

3 Science Drive 3, Singapore 117543

Website: www.chemistry.nus.edu.sg

Company Registration No: 200604346E

Green Chemistry Accepted Manuscript

Website: www.chemistry.nus.edu.sg

Company Registration No: 200604346E

ARTICLE

Single-atom photocatalysis for sustainable organic synthesis: a critical review

Received 00th January 20xx,
Accepted 00th January 20xx

DOI: 10.1039/x0xx00000x

Yang Shi,†[a] Wei Fang,†[a] Gan Wang,[a] Guangmei Gan[b] and Jie Wu*[a]

Single-atom catalysts (SACs) have recently emerged as a powerful platform for heterogeneous photocatalysis owing to their atomically dispersed active sites, well-defined coordination environments, and tunable electronic structures. These characteristics enable efficient light-driven transformations with high selectivity and near 100% theoretical metal atom utilization. In recent years, SAC-based photocatalytic systems have demonstrated remarkable performance in diverse energy-related reactions, including hydrogen evolution, CO_2 reduction, and selective oxygen reduction. More recently, their application has rapidly expanded into photocatalytic organic synthesis under mild and sustainable conditions. This review provides a comprehensive overview of recent advances in SAC-mediated photocatalytic organic transformations. Reaction types including coupling, addition, functional group oxidation, and others are systematically summarized with emphasis on catalytic mechanisms, substrate scopes, and structure-activity relationships. Particular attention is given to the unique role of isolated metal atoms in regulating charge separation, radical generation, and single-electron transfer (SET) processes. Finally, current challenges and future opportunities are discussed. These insights highlight the potential of SACs as cornerstone materials for sustainable photocatalytic organic synthesis.

Green foundation

1. This review highlights single-atom photocatalysis as a sustainable platform for organic synthesis. By maximizing metal atom utilization and enabling light-driven reactions under mild conditions, SAC-based systems significantly reduce metal waste, energy consumption, and reliance on stoichiometric reagents compared with traditional catalytic redox approaches.
2. Photocatalytic organic transformations mediated by SACs align closely with several principles of green chemistry, including atom economy, energy efficiency, minimized waste, and catalyst recyclability. The heterogeneous nature of SACs facilitates catalyst recovery and reuse while avoiding issues associated with homogeneous metal complexes.
3. The mechanistic insights and catalyst-design strategies summarized in this review, such as coordination environment engineering, defect regulation, and cooperative multi-site catalysis provide guidance for developing next-generation photocatalytic systems, accelerating the transition toward greener and more sustainable chemical synthesis.

1. Introduction

Single-atom catalysts (SACs) represent a distinctive class of catalytic materials, characterized by atomically dispersed metal atoms anchored on solid supports. Their defining features include atomically precise dispersion, structurally uniform active sites, and well-defined coordination environments. Since the seminal concept was proposed in 2011, SACs have garnered tremendous research interest owing to their near 100% atom utilization, finely tunable electronic structure, well-defined catalytic site analogous to homogeneous molecular catalysts and exceptional catalytic selectivity.[1] In contrast to conventional metal nanoparticles, single-atom sites possess discrete electronic states, enabling precise modulation of key parameters such as oxidation state, d-orbital occupancy, and adsorption behaviour toward reaction intermediates. Such control can be achieved through rational design of the support composition, coordinating atoms (e.g., C, N, and O), and defect engineering (Fig. 1a).[2–5] This atomic-level precision not only underpins the outstanding catalytic performance of SACs but also renders them ideal model systems for elucidating reaction mechanisms and structure-performance relationships.

These unique characteristics are particularly advantageous in photocatalysis, a field often challenged by rapid charge recombination, sluggish interfacial charge transfer, and ill-defined active sites.[6] In most SAC-based photocatalytic systems, the semiconductor support serves as the primary light-harvesting component, while the isolated metal atoms function as electronic modulators, introducing mid-gap states and/or promote interfacial charge transfer through metal-support interactions.[7] The photocatalytic activity therefore primarily originates from the electronic coupling between the isolated metal atoms and the semiconductor support, which may involve ligand-to-metal charge transfer (LMCT) or metal-to-ligand charge transfer (MLCT) processes, rather than from direct photoexcitation of the metal atoms themselves. Building on this, localized electric fields at semiconductor interfaces will be generated to promote spatial separation of electrons and holes while suppressing recombination.[8] In addition, strong metal-support interactions (SMSI) or covalent coordination

[a] Department of Chemistry, National University of Singapore, 3 Science Drive 3, Singapore 117543, Singapore.
[b] School of Resources and Environmental Engineering, Wuhan University of Technology, Wuhan, Hubei, China.
† These authors have equal authorship.

Green Chemistry Accepted Manuscript

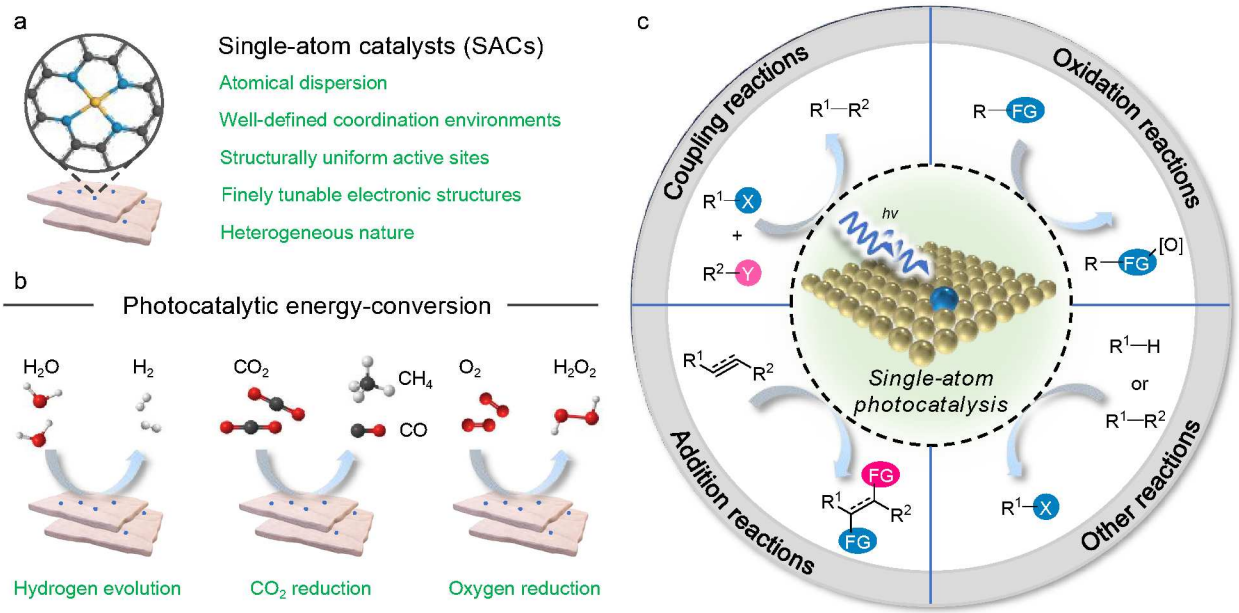

Fig. 1 (a) The definition and characteristics of single-atom catalysts (SACs). (b) Photocatalytic energy-conversion applications of SACs. (c) Photocatalytic organic synthesis employing SACs.

environments enable directional electron-transfer pathways, substantially accelerating charge migration to reactive centers. Importantly, the isolated metal atoms typically exhibit moderate binding affinities toward key intermediates (e.g., *H, *COOH, *CO, $*O_2^-$), thereby lowering activation barriers while mitigating catalyst deactivation associated with excessively strong adsorption.[7]

From a green and sustainable chemistry perspective, photocatalysis offers distinctive advantages over thermal processes. Harnessing light as a renewable and traceless energy input allows reactions at ambient temperature and pressure, reducing the energy consumption and carbon footprint. More importantly, photoexcitation generates reactive intermediates *via* single-electron transfer (SET) or energy transfer (EnT) mechanisms, which in most cases circumvents the use for hazardous oxidants, reductants, or radical initiators.[9] When combined with heterogeneous catalysis, the sustainability advantages are further amplified. Unlike homogeneous catalysts that require laborious separation and pose a risk of metal contamination, heterogeneous photocatalysts can be readily recovered and reused, reducing precious metal consumption and simplifying purification.[10] This recyclability also improves E-factors and process mass intensity (PMI) profiles.[11] Single-atom photocatalysts, with their heterogeneous nature, ideally integrate these advantages with molecular-level precision.

Benefiting from these advantages, SACs have demonstrated remarkable performance in diverse photocatalytic energy-conversion processes, including hydrogen evolution, CO_2 reduction, and selective oxygen reduction to H_2O_2 (Fig. 1b).[12-15] Concurrent advances in *in situ* spectroscopy and density functional theory (DFT) calculations are providing unprecedented insights into the dynamic evolution of SACs under operating conditions, steering the field from empirical optimization toward rational catalyst design.[16]

Photocatalytic organic transformations have been explored using homogeneous photocatalysts, including metal complexes, metal-free organic dyes (e.g., acridinium salts, eosin Y, and benzophenone derivatives),[17] and heterogeneous systems, such as metal nanoparticles doped or metal-free semiconductors (e.g., pristine carbon nitride).[18] While homogeneous photocatalysts often face challenges associated with catalyst separation and long-term stability, heterogeneous photocatalysts may suffer from limited activity, inefficient charge separation, and poorly defined active sites.[19] In contrast, SACs offer a compelling platform that bridges the gap between molecular catalysts and heterogeneous materials, combining high selectivity with operational robustness. This field has advanced rapidly in recent years and demonstrated its effectiveness in a broad spectrum of photoinduced organic transformations, including coupling reactions (C–C, C–N, C–O bond formations), selective oxidation, hydrogenation and addition reactions (Fig. 1c). The ability of single-atom sites to precisely modulate single-electron transfer processes is widely regarded as a key factor underpinning the high chemo- and regioselectivity observed in these reactions.[20] In this context, the present review provides a comprehensive overview of recent advances in SAC-mediated photocatalytic organic synthesis, with particular emphasis on reaction types, substrate compatibility and mechanistic insights. While previous reviews have thoroughly surveyed SACs in organic synthesis, the emerging photo-driven branch has received less systematic attention.[20-22] This review complements those works by focusing on distinct mechanistic roles of isolated metal sites in

Green Chemistry Accepted Manuscript

This journal is © The Royal Society of Chemistry 20xx

photocatalysis, which extend beyond substrate activation to the regulation of photogenerated charge-carrier dynamics and SET pathways. We further highlight advances from 2024 to 2026 that have not been covered in earlier surveys. In terms of material scope, this review primarily focuses on heterogeneous supports, including carbon nitrides (CN, a general term encompassing graphitic carbon nitride (g-C_3N_4), polymeric carbon nitride (PCN), and nitrogen-doped carbon (CN_x)), metal oxides, metal sulfides, carbon-based materials, and related semiconductors. Covalent organic framework (COF) and metal-organic framework (MOF)-based systems, which possess periodically linked frameworks and predesigned pore-confined coordination environments, are considered a distinct platform and are beyond the main scope of this review.

2. Coupling reactions

Since the recognition of transition-metal-catalyzed cross-coupling reactions with the Nobel Prize in Chemistry in 2010, this field has attracted sustained and widespread interest, constituting a central strategy for constructing C–C and C–heteroatom bonds, underpinning the synthesis of complex molecules ranging from pharmaceuticals to functional materials. While homogeneous metal catalysts remain indispensable in coupling chemistry, challenges associated with catalyst separation, recovery, and residual metal contamination remain significant.. Photocatalysis offers a promising alternative for driving coupling reactions under mild conditions, while the incorporation of isolated metal sites into heterogeneous semiconductor supports offers additional advantages, including facile catalyst recovery and high selectivity. In many cases, the SAC heterogeneous systems exhibit minimum metal leaching even after long reaction duration. In this review, coupling reactions are systematically classified into three categories according to the mechanistic characteristics (net electron flow) and substrates: oxidative couplings, reductive couplings, and redox-neutral couplings (Fig. 2a).

2.1 Oxidative coupling reaction

In a conventional oxidative coupling reaction, an external oxidant is typically required, in which stoichiometric or excess quantities of metal salts (e.g., Cu or Ag salts), hypervalent iodine reagents, or peroxides are frequently employed.[23] Such practices inevitably compromise atom economy and sustainability. In contrast, this long-standing limitation has been greatly mitigated by single-atom photocatalytic systems. Owing to their intrinsic band structures, photoexcitation generates electron-hole pairs that impart redox functionality to the catalyst, enabling either direct substrate oxidation by photogenerated holes or indirect oxidation with reactive oxygen species (ROS) *via* the reduction of molecular oxygen.

In 2020, Zhao and co-workers reported a representative study based on CN hollow spheres (HCNSs) decorated with Cu single atoms.[24] By controlling the spatial location of Cu species, embedded Cu1@HCNS and surface-loaded Cu1/HCNS model catalysts were constructed. Systematic comparison revealed an unconventional role of single atoms: embedded Cu–N_3 sites do not serve as direct catalytic centers but instead act as electronic modulators. This conclusion was supported by the lower benzylamine oxidation activity of surface-loaded Cu1/HCNS (2807 $\mu mol \cdot g^{-1} \cdot h^{-1}$) than bare HCNS (4267 $\mu mol \cdot g^{-1} \cdot h^{-1}$), the negligible H_2 evolution over Cu1@HCNS without a Pt cocatalyst, and the most efficient charge separation observed for Cu1@HCNS in photoluminescence (PL), time-resolved PL, electrochemical impedance, and transient photocurrent measurements. These sites broaden visible-light absorption, promote interfacial charge transfer, and effectively suppress charge-carrier recombination, leading to a pronounced spatial-position effect. As a result, Cu1@HCNS simultaneously exhibits efficient photocatalytic H_2 evolution and anaerobic oxidative coupling of benzylamines to imines under visible light, with substrate tolerance toward halogen-, alkyl-, and alkoxy-substituted benzylamines and a maximum oxidation rate of 11242 $\mu mol \cdot g^{-1} \cdot h^{-1}$. Mechanistic studies suggest that photogenerated holes induce hydroxyl-radical formation, while electrons drive proton reduction, collectively enabling imine formation and H_2 evolution (Fig. 2b).This work uniquely reveals that the spatial location of single-atom sites, whether embedded within the support or anchored on its surface, can fundamentally dictate photocatalytic behaviour, expanding SAC design principles beyond the conventional emphasis on metal identity alone.

Beyond CN, carbon-supported single-atom catalysts have also been applied to benzylamine oxidation. In 2020, Li et al. developed a Co single-atom catalyst on carbon quantum dots (CoSAS@CD) for visible-light-driven oxidative coupling of benzylamines to imines under oxygen (Fig. 2c).[25] The reaction proceeds with up to 99% conversion and selectivity, tolerates diverse substituents, and notably enables cross-oxidative coupling between benzylamines and aliphatic primary amines. In this work, photogenerated holes and ROS, including $^1O_2$ and $\cdot O_2^-$, cooperatively promote amine oxidation and C–N bond formation, highlighting the synergy between light harvesting and single-atom active sites.

Similarly, Li and co-workers further developed a porphyrin-based porous organic cage hosting cobalt single-atom catalyst (CoP@POC).[26] The porphyrin units feature strong and tunable visible-light absorption, while their intrinsic N_4 coordination environments stabilize Co single atoms within the cage, striking a balance between structural robustness and charge-transport efficiency. Under visible light and oxygen, CoP@POC promotes the selective oxidative coupling of benzylamines to imines with conversions and selectivity near 99% and a turnover frequency (TOF) as high as 1389 h^{-1}. The system exhibits good substrate compatibility, excellent recyclability and photostability (Fig. 2d).

In 2022, Li et al. reported a single-atom photocatalyst by anchoring atomically dispersed Pd on $ZnIn_2S_4$ nanosheets (PdSA-ZIS).[27] The Pd single atoms induce spatial charge separation, enabling electron accumulation at Pd sites for proton reduction and hole localization in sulfide regions for oxidation. As a result, PdSA-ZIS efficiently promotes

Green Chemistry Accepted Manuscript

photocatalytic dehydrogenative coupling of benzylamines to *N*-benzylidenebenzylamine with nearly quantitative selectivity,

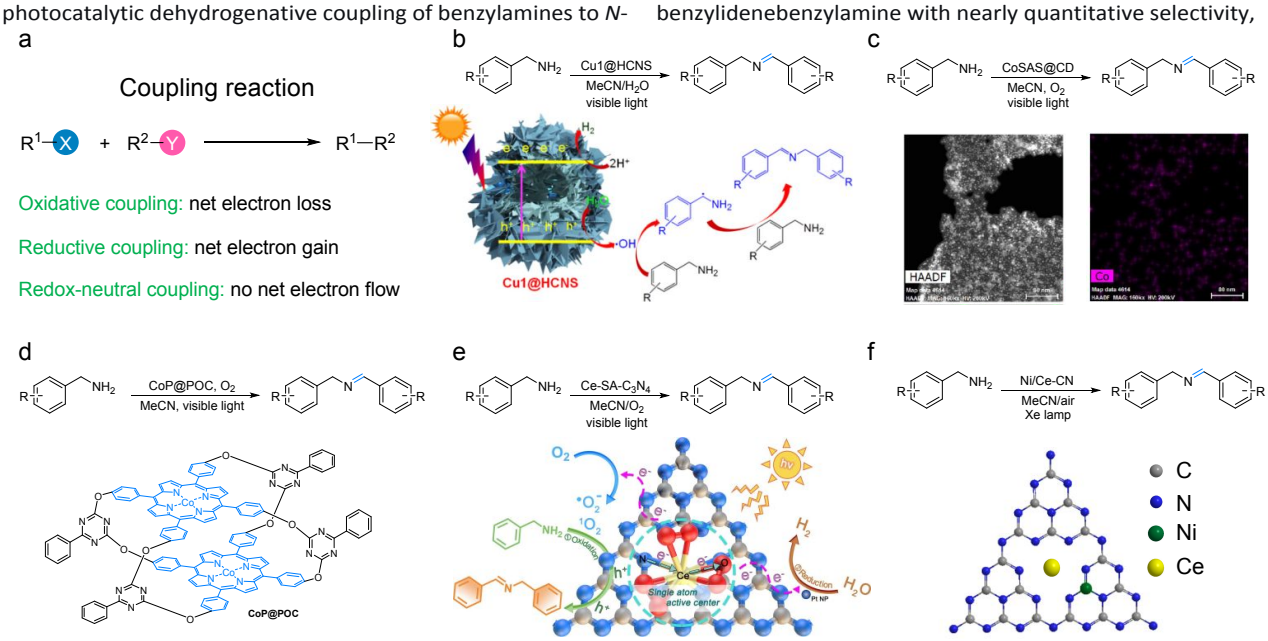

Fig. 2 (a) Three categories of coupling reaction. (b) Cu1@HCNS for photocatalytic oxidative coupling of benzylamines to imines. Reproduced with permission.[24] Copyright 2020, American Chemical Society. (c) CoSAS@CD for oxidative coupling of benzylamines to imines. Reproduced with permission.[25] Copyright 2020, American Chemical Society. (d) The structure and the application of CoP@POC. Reproduced with permission.[26] Copyright 2020, American Chemical Society. (e) Schematic illustration of Ce-SA-C_3N_4 for oxidative coupling of benzylamines. Reproduced with permission.[28] Copyright 2023, Elsevier. (f) Ni/Ce-CN photocatalytic C–N coupling. Reproduced with permission.[29] Copyright 2024, Springer Nature.

accompanied by H_2 evolution. Subsequently, control experiments, DFT calculations, and *in situ* electron spin resonance (ESR) spectroscopy confirm that photogenerated holes initiate benzylamine dehydrogenation to amine radical intermediates, while electrons at Pd single atoms drive proton reduction. The rapid generation and consumption of radical intermediates are key to achieving high C–N coupling selectivity through synchronized oxidative and reductive half-reactions.

Beyond transition-metal SACs, Tian et al. reported a highly coordinated cerium single-atom-modified CN (Ce-SA-C_3N_4), in which Ce atoms are stabilized in Ce-N_4/O_6 coordination environments, showcasing that rare-earth based SACs also feature unique potential in photocatalytic oxidative coupling.[28] In this work, these Ce sites can modulate the local electronic structure and introduce beneficial surface trap states, promoting charge separation and migration. Simultaneously, enhanced O_2 adsorption and activation enable efficient and selective oxidative coupling of benzylamines to imines, functional groups including methoxy, alkyl, halogen and trifluoromethyl can be tolerated (Fig. 2e), while a TOF as high as 738.1 h^{-1} has been achieved. The distinctive Ce–N_4/O_6 coordination environment of this rare-earth SAC differs markedly from the commonly reported M–N_4 motifs, suggesting that coordination-number engineering provides an additional dimension for regulating the electronic structure and photocatalytic behaviour of single-atom sites.

In 2024, Tian et al. further reported a defect-rich Ni/Ce co-doped CN (Ni/Ce-CN) photocatalyst for visible-light-driven oxidative coupling of primary amines to imines under air.[29] Compared with undoped or singly doped CN, Ni/Ce-CN shows enhanced reaction rates and higher conversions (31% for CN; 87% for Ce-CN; 91% for Ni-CN; 99% for Ni/Ce-CN), together with broad substrate scope and good recyclability. The improved performance is attributed to synergistic Ni/Ce doping and defect sites (Fig. 2f). Distinct from conventional single-atom systems, this work highlights bimetallic co-doping as an alternative strategy for harnessing the complementary electronic properties of transition metals (Ni) and rare-earth metals (Ce) sites to enhance photocatalytic performance through cooperative effects.

Beyond homocoupling of benzylamine, Ni single atoms anchored on CN (Ni-SA@PCN), which was prepared *via* a microwave-reduction procedure using bulk PCN and $Ni(NO_3)_2$ (Fig. 3a), also enable oxidative cross-coupling between aromatic alcohols (**1**) and aliphatic amines (**2**) to form imines.[30] This system demonstrates excellent compatibility with various substituted aromatic alcohols bearing electron-withdrawing (**3b**-**c**) and electron-donating groups (**3d**) as well as aliphatic amines with different chain lengths (**3e**-**f**). Imine selectivity consistently exceeds 99%, while overoxidation and side reactions are effectively suppressed, reflecting the high chemoselectivity and good tolerance (Fig. 3b). Mechanistically, this reaction proceeds through a distinct pathway compared with the benzylamine homocoupling discussed above. The reaction is initiated by photogenerated hole-driven oxidation of

Green Chemistry Accepted Manuscript

This journal is © The Royal Society of Chemistry 20xx

the aromatic alcohol to the corresponding aldehyde, identifying as the rate-limiting step, followed by condensation with the

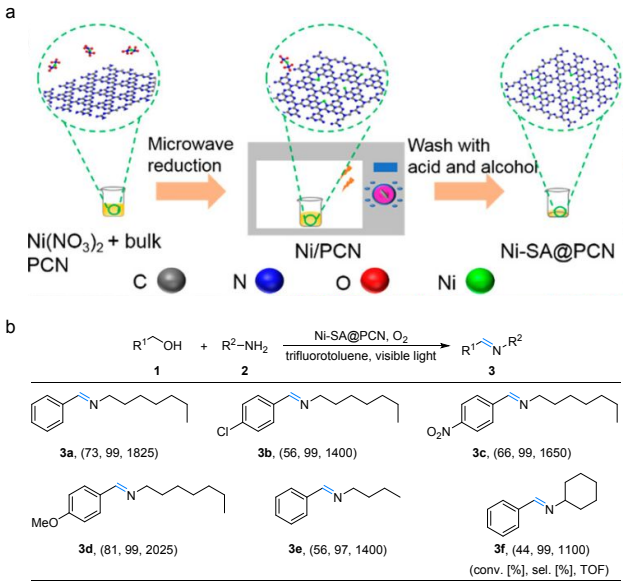

Fig. 3 (a) The preparation of Ni-SA@PCN. Reproduced with permission.[30] Copyright 2022, American Chemical Society. (b) Selected examples of the photocatalytic cross-coupling of alcohols and amines.

aliphatic amine and dehydration to afford the imine product. Radical trapping experiments and electron paramagnetic resonance (EPR) spectroscopy further revealed that singlet oxygen ($^1O_2$) and superoxide (O_2^-), generated *via* electron transfer to molecular O_2, are the predominant ROS, whereas ·OH plays a negligible role.

Compared to alkylamines, the *α*-C–H bond of ketones is often more difficult to oxidize due to the electron-deficient nature. Two representative studies in 2020 and 2023 based on single-atom Pt-TiO_2 photocatalysis for the homocoupling of acetone have been reported.[31,32] These works systematically revealed the critical role of Pt-TiO_2 single atom photocatalyst in activating inert *α*-C–H bonds and facilitating oxidative coupling reactions. Specifically, in 2020, Guo et al. demonstrated that Pt single atoms supported on TiO_2 enable photoinduced *α*-C–H dehydrogenation of acetone under 300 W Xe lamp equipped with IR light filters, generating $\cdot CH_2COCH_3$ radicals that undergo homocoupling to form 2,5-hexanedione (HDN) selectively, with H_2 evolution as the reductive half-reaction.[31] Comparative studies revealed that Pt single atoms are indispensable for radical generation, while C–C bond formation proceeds *via* free-radical recombination rather than on metal sites, establishing a reaction model in which single atoms promote initial C–H activation. In 2023, Lin et al. further elucidated this system by emphasizing the role of the Pt-TiO_2 interface.[32] Through controlled Pt dispersion, *in situ* spectroscopy, and DFT calculations, Pt cluster is identified as a better electron-enrichment center than single atom, facilitating directional electron transfer, lowering the barrier for acetone *α*-C–H activation, and stabilizing key radical intermediates, thus improving reaction selectivity.

Furthermore, single-atom photocatalytic strategy has been successfully applied in the coupling of inert small molecules. For instance, Wang et al. investigated a dual-phase ZnCdS nanorod system with precisely anchored Rh single atoms.[33] The built-in electric field generated by the periodic wurtzite and cubic zinc-blende (WZ/ZB) heterojunction enabled directional spatial separation of photogenerated electrons and holes (Fig. 4a), while the single-atom Rh sites are selectively anchored in the hole-enriched region, significantly lowering the activation barrier for the cleavage of C–H bond in methanol and promoting the formation of $\cdot CH_2OH$ radicals. Consequently, this system achieved efficient photocatalytic coupling of methanol to ethylene glycol (EG) under sacrificial agent free conditions, demonstrating the feasibility of steering reaction pathway selectivity through precise structural engineering and site-specific single-atom regulation.

Notably, some reactions described as “non-oxidative coupling” can be mechanistically classified as photocatalytic oxidative coupling. For example, Long et al. reported a Pt single-atom nest photocatalyst (T-Pt_{SAs}-N) for methane coupling in 2024, in which Pt single atoms are situated in neighbouring regions with approximately 4 Å distance (Fig. 4b).[34] Although no molecular oxygen is involved, the reaction proceeds *via* photoinduced C–H dehydrogenation of methane followed by C–C coupling, with proton reduction and H_2 evolution as the reductive half-reaction. This process is therefore more appropriately described as hydrogen-evolution oxidative coupling like above mentioned examples. The precisely arranged multiple Pt single atoms cooperatively promote initial C–H activation while suppressing deep oxidation and carbon deposition. As a result, a C_2H_6 yield of 251.6 μmol $g_{cat}^{-1}\cdot h^{-1}$ and TOF of 20 h^{-1} have been achieved. This work highlights how spatial organization of single atoms regulates C–H activation pathways and coupling efficiency.

Furthermore, biomimetic single-atom photocatalysts provide innovative strategies for complex organic transformations. By covalently anchoring hemin molecules onto CN surfaces (Fig. 5a), Wang et al. developed a bio-inspired single-atom Fe photocatalyst for sulfonylation of alkenes under visible light and air.[35] In this system, the Fe center adopts a well-defined Fe–N_4 coordination environment derived from the hemin porphyrin framework, with high-angle annular dark-field scanning transmission electron microscopy

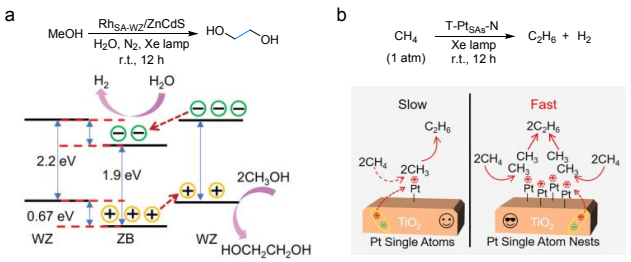

Fig. 4 (a) Scheme for the formation of H_2 and EG by photogenerated electrons and holes. Reproduced with

Green Chemistry Accepted Manuscript

permission.[33] Copyright 2023, John Wiley and Sons. (b) Schematic diagram of photocatalytic methane coupling over Pt single-atoms and Pt single-atoms nests. Reproduced with permission.[34] Copyright 2024, American Chemical Society.

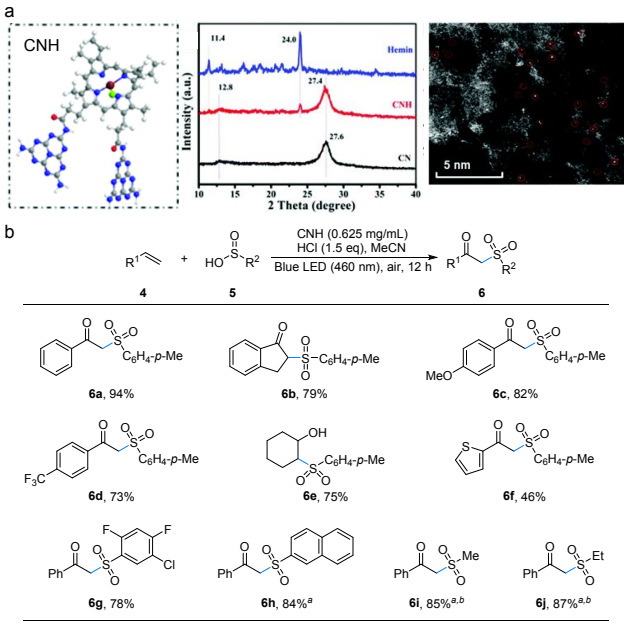

Fig. 5 (a) Schematic representation of the CNH photocatalyst. Reproduced with permission.[35] Copyright 2020, The Royal Society of Chemistry. (b) Selected examples of the photocatalytic sulfonylation of alkenes.

(HAADF-STEM) confirming the atomic dispersion of Fe and inductively coupled plasma mass spectrometry (ICP-MS) revealing an Fe loading of 0.646 mmol g^{-1}. The covalent coupling of hemin to CN not only extends the visible-light absorption range but also promotes charge separation through energy-level alignment between the semiconductor support and the Fe–N_4 sites. As a result, CN functions as the light-harvesting and charge-separation unit, while the Fe single-atom site mimics enzymatic active centers to activate oxygen and generate radicals. The synergy between light-harvesting CN and catalytically active Fe–N_4 sites enables broad substrate compatibility in photocatalytic alkene sulfonylation. Both terminal and internal alkenes bearing electron-donating or electron-withdrawing substituents undergo efficient transformation (**6a–d**), with the reaction also accommodating non-conjugated olefins (**6e**). The scope further extends to sulfinic acids containing halogen or alkyl substituents (Fig. 5b).

In 2025, Cai, Rueping, and co-workers developed an atomically dispersed cobalt single-atom photocatalyst (Co_{SA}-K-PHI) *via* a mild Co/K ion-exchange strategy on ionic CN K-PHI (Fig. 6a).[36] By integrating the light-harvesting unit and isolated Co^{2+} sites within a rigid framework, photogenerated holes and electrons are efficiently directed to oxidative radical generation and reductive single-atom-mediated steps, respectively, enabling effective radical coupling under mild conditions. Subsequently, this catalyst was applied to a decarboxylative Heck-type coupling, using carboxylic acids (**7**) and alkenes (**8**) to construct multi-substituted olefins (**9**). The reaction achieves selective C(sp^3)–C(sp^2) bond formation under heterogeneous conditions without noble metals, while delivering yields and selectivity comparable to homogeneous systems with low catalyst loading (Fig. 6b). Wide substrate scope, good functional-group tolerance (applicable to the late-stage functionalization and synthesis of complex natural products or drug precursors), and catalyst recyclability (at least six times) further underscore the practical potential of this single-atom photocatalytic platform.

In the same year, Wu and co-workers reported a novel hydrogen-evolution cross-dehydrogenative couplings (CDCs) driven by a single-atom catalyst.[37] In this work, platinum is anchored as isolated atoms on a CN support, achieving maximized active-site exposure while minimizing metal consumption (Fig. 7a). This unique structural design not only enhances the separation efficiency of photogenerated charge carriers but also enables the Pt single atoms to function as electron traps, promoting proton reduction and H_2 evolution, thereby coupling the oxidative coupling process with H_2 generation under light irradiation. Notably, $Zn(OTf)_2$ is essential for the reaction, as its absence resulted in a substantial decrease in yield to only 14%. Based on the CV measurements, additive screening and photocurrent measurements, the role of $Zn(OTf)_2$ as a Lewis acid is ruled out. Instead, $Zn(OTf)_2$ is proposed to stabilize the transient radical cation intermediates and works as a buffering agent to suppress the electron-hole recombination. This integration of light-absorption functionality with single-atom active sites breaks through the traditional limitation of CDC reactions that rely on pre-functionalized substrates (e.g., halogenated arenes) and external oxidants, significantly simplifying synthetic routes and improving atom economy. Experimental results demonstrated

Green Chemistry Accepted Manuscript

This journal is © The Royal Society of Chemistry 20xx

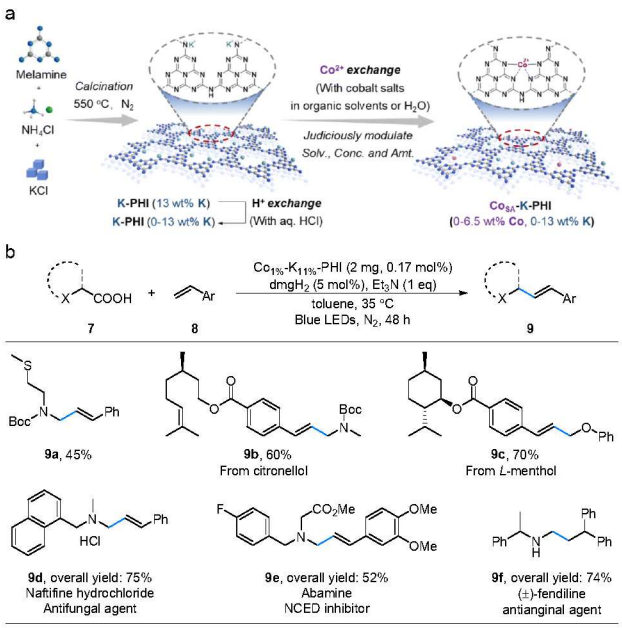

Fig. 6 (a) Schematic representation of the Co_{SA}-K-PHI design and preparation. Reproduced with permission.[36] Copyright 2025, The Royal Society of Chemistry. (b) Selected examples of the photocatalytic decarboxylative Heck-type coupling.

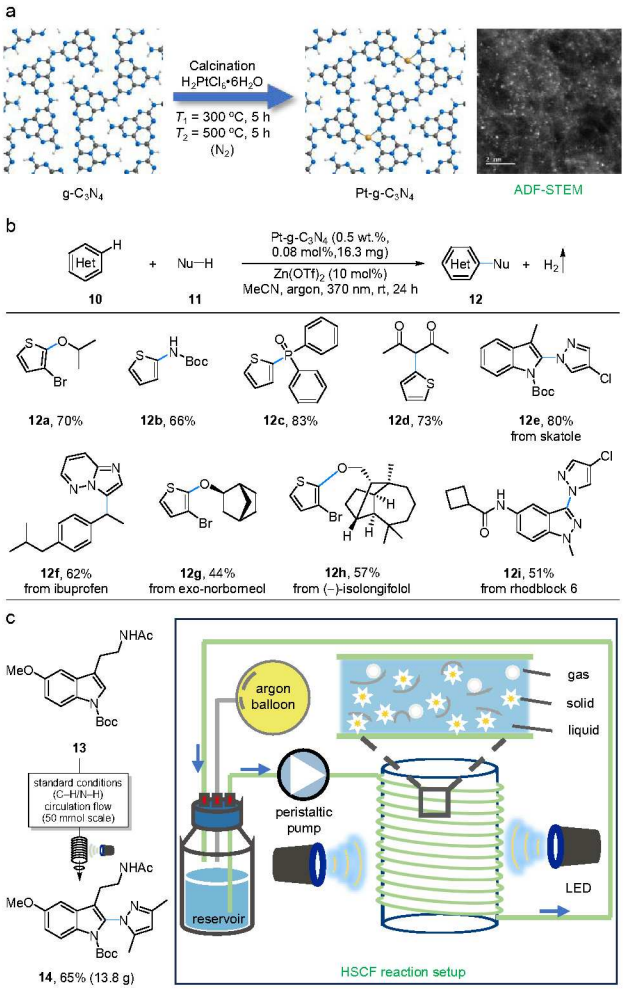

Fig. 7 (a) Schematic preparation of Pt-g-C_3N_4 and annular dark-field scanning transmission electron microscopy (ADF-STEM) of SAC. (b) Selected examples of the photocatalytic CDC reactions between (hetero)arenes and nucleophiles. (c) 10-gram-scale circulation flow synthesis. Reproduced with permission.[37] Copyright 2025, Springer Nature.

that upon 370 nm irradiation, the system accommodates a wide range of (hetero)arenes (thiophene, furan, indole, pyrrole, Imidazo[1,2-*b*]pyridazine, indazole, benzene and pyridine) and diverse nucleophiles (alcohol, pyrazole, carbonate, disulfonimide, diarylphosphine oxide, 1,3-dicarbonyl compound, and carboxylic acid), producing C–O, C–N, C–P, and C–C coupling products in moderate to excellent yields, accompanied by H_2 formation. Moreover, the system shows practical utility in late-stage functionalization of natural products, drug molecules, and optoelectronic functional compounds (Fig. 7b), as well as a 10-gram-scale synthesis of melatonin derivative **14** in 65% yield with high-speed circulation flow (HSCF) technology, which represent an excellent platform for heterogeneous photocatalysis with good tolerance of solids in flow (Fig. 7c),[38] while exhibiting excellent catalyst recyclability and stability. Overall, this protocol adheres to most of the

Green Chemistry Accepted Manuscript

twelve principles of green chemistry and underscores the promise of single-atom photocatalysts for hydrogen-evolution-coupled CDC transformations in sustainable catalysis.

2.2 Reductive coupling reaction

In contrast to oxidative coupling reactions, reductive coupling reactions employing single-atom photocatalytic systems predominantly rely on the directional accumulation and transfer of photogenerated electrons to activate electrophilic substrates, unsaturated intermediates, or C1 feedstocks, enabling bond formation through a reductive pathway. In such processes, isolated metal atomic sites typically function as highly efficient electron sinks, preferentially capturing and stabilizing photogenerated electrons upon semiconductor excitation.[39] This capability facilitates the formation of reactive low-valent metal species or metal-radical intermediates under mild conditions. As a result, single-atom photocatalysts exhibit distinct advantages in the reductive activation of aryl halides, alkyl halides or other electrophiles.[13,39] Different from oxidative coupling reactions using ROS, reductive coupling generally offers enhanced functional-group tolerance and more predictable control over coupling site selectivity.[40]

In 2022, the Reisner group developed an integrated nickel-CN (Ni-mpg-CN_x) photocatalyst as a fully heterogeneous platform for the light-driven amination coupling of aryl halides (**15**) with sodium azide **16**.[41] This system circumvents the need for sophisticated ligands and precious metals. Synergistic interactions between the CN framework and Ni sites enable cross-coupling of a wide range of aryl and heteroaryl bromides with NaN_3 under mild conditions (Fig. 8a). Notably, although the original study did not explicitly identify the Ni sites as single atoms, spectroscopic analysis indicated coordination of Ni^{2+} species with pyridinic N sites, and DFT calculations based on a single-atom Ni model within the mpg-CN_x matrix were employed to rationalize the catalytic mechanism, consistent with atomically dispersed Ni sites. The dominant side reactions are limited to minor dehalogenation products, the corresponding phenols, and solvent-derived aryl ethers. Substrates bearing nitrile, ketone, ester, amide, sulfone, and trifluoromethyl groups afford products in good to excellent yields (**17a**-**l**, 65-86%);electron-neutral and electron-rich aryl bromides are also compatible, albeit with slower reaction kinetics (**17m**-**n**). Aryl iodides are reactive but more prone to dehalogenation (up to 20%), whereas aryl chlorides show markedly diminished reactivity (< 25% yield) owing to the stronger C–Cl bond. After the reaction, the catalyst can also be simply reused for several cycles without significant decrease in yield, despite slight Ni aggregation (Fig. 8b).

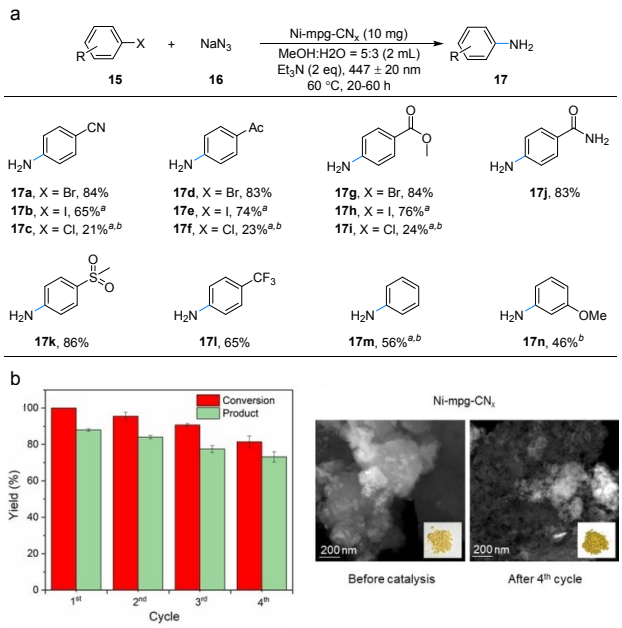

Fig. 8 (a) Selected examples of the photocatalytic reductive coupling between aryl bromides with NaN_3. (b) Recycling experiments and HAADF-STEM images of Ni-mpg-CN_x before and after reactions. Reproduced with permission.[41] Copyright 2022, John Wiley and Sons.

Subsequently in 2024, Hu and co-workers reported a photocatalyst based on ultrathin TiO_2(B) nanosheets decorated with Cu single atoms and oxygen vacancies. The ultrathin two-dimensional morphology, with a thickness of approximately 1.0-1.5 nm, shortens the charge-carrier migration distance from the bulk to the surface, thereby minimizing bulk recombination and promoting interfacial charge transfer and subsequent surface redox reactions.[42] With UV-visible-light irradiation (λ > 365 nm), this system efficiently promotes dehalogenative C–C homocoupling of benzyl bromide to bibenzyl, outperforming visible-light condition (Fig. 9a), pristine TiO_2 and single-site catalysts in activity and selectivity. Mechanistic studies indicate that oxygen vacancies facilitate C–Br bond activation and substrate adsorption, while isolated Cu atoms enhance charge separation and directional electron transfer.

In the same year, Zhao and co-workers reported a Pt-Bi bimetallic, oxygen-vacancy-rich CeO_{2-x} photocatalyst for the *N*-formylation of amine using CO_2 as a C1 source.[43] Under Xe lamp irradiation with phenylsilane as reductant, *N*-methylaniline was converted nearly quantitatively within 3 h, affording *N*-methylformanilide with near 90.8% selectivity. Mechanistic studies indicate the formation of adsorbed HCOO* radical as key intermediate and silanol as terminal byproduct (Fig. 9b). The reaction is applicable to aromatic amines as well as aliphatic amines such as morpholine and *n*-butylamine, while maintaining high conversions and selectivity. In addition, good recycling stability of the catalyst is also observed.

Then, Zhou and Cao reported a photocatalytic system based on Pt single atoms anchored on graphitic frameworks (Pt/GFs) for the hydrogenative cyclization of levulinic acid (LA) to γ-valerolactone (GVL) (Fig. 9c).[44] The isolated Pt sites promote charge separation and facilitate hydrogen transfer and subsequent C–O/C–C bond reorganization, enabling highly selective LA to GVL conversion under visible-light irradiation.

Recently, Wu, Li, Ma, and co-workers reported a CN photocatalyst featuring a high density of atomically dispersed Pd single atoms (Pd_{SA}-PCN), prepared *via* a two-step annealing strategy that preserves atomic dispersion at elevated Pd

Green Chemistry Accepted Manuscript

This journal is © The Royal Society of Chemistry 20xx

loadings.[45] Structural characterizations confirm that Pd incorporation modulates the band structure of CN, enhancing charge transfer while retaining its intrinsic water oxidation capability. Based on this platform, a light-induced tandem decarbonylation/carbonylative reductive coupling reaction was developed. Aryl iodides (**18**) act as electrophiles, while pivaldehyde **19** serves as an *in situ* CO source through aldehyde decarbonylation, followed by CO migration between adjacent Pd sites, insertion, and reductive coupling (Fig. 10a).

Distinct from conventional carbonylation reactions requiring high-pressure CO or specialized CO surrogates and sacrificial metals, this method operates under ambient pressure and irradiation, using water as the sole reductant. Consequently,

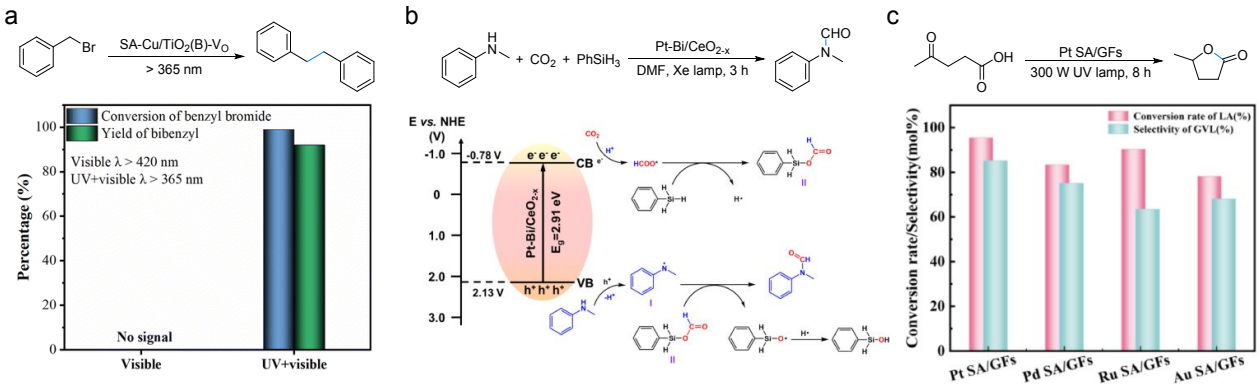

Fig. 9 (a) Photocatalytic performance for dehalogenative C–C homocoupling of benzyl bromide under visible (λ > 420 nm) and UV-visible light (λ > 365 nm) irradiation, respectively. The blue bars represent the conversion of benzyl bromide, and the green bars represent the yield of bibenzyl; the y-axis therefore indicates the corresponding percentage values. Reproduced with permission.[42] Copyright 2024, The Royal Society of Chemistry. (b) A possible mechanism of the photocatalytic CO_2 *N*-formylation of *N*-methylaniline. Reproduced with permission.[43] Copyright 2024, Elsevier. (c) Schematic illustration of Pt/GFs for photocatalytic hydrogenative cyclization of levulinic acid (LA). Reproduced with permission.[44] Copyright 2025, Elsevier.

Green Chemistry Accepted Manuscript

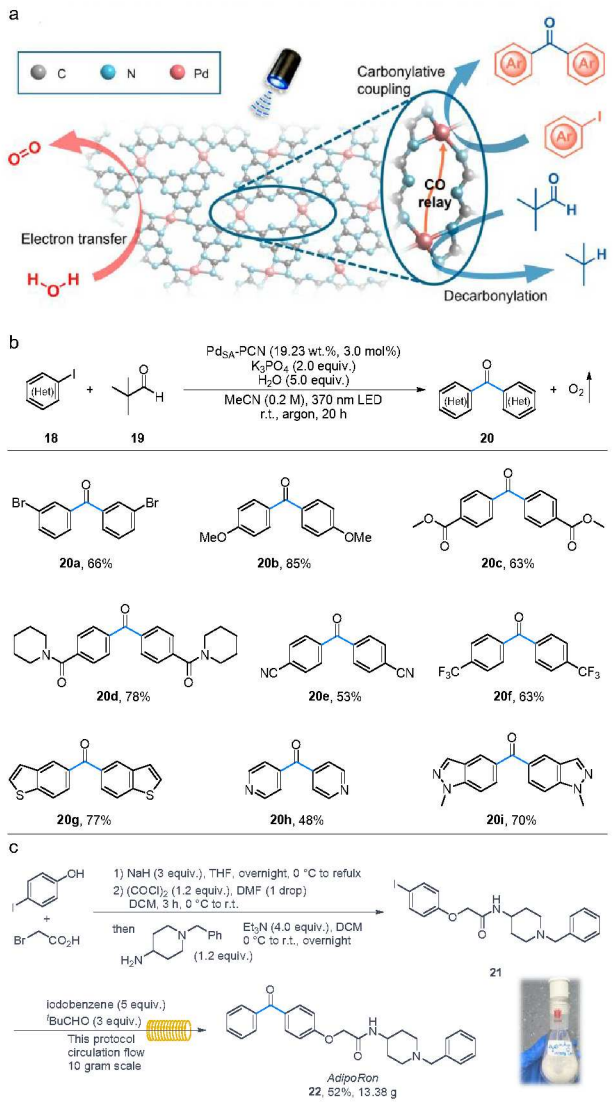

Fig. 10 (a) Schematic illustration of Pd_{SA}-PCN for reductive coupling between aryl iodides with pivaldehyde. (b) Selected examples of substrate scope. (c) 10-gram-scale circulation flow synthesis. Reproduced with permission.[45] Copyright 2025, American Chemical Society.

the protocol exhibits markedly improved safety, atom economy, and sustainability. The methodology is applicable to a variety of aryl iodides with diverse functional groups including halides, ethers, esters, amides, nitriles, and trifluoromethyl groups and heteroaromatic frameworks (Fig. 10b). Notably, the late-stage functionalization of pharmaceutical molecules and a decagram-scale circulation-flow synthesis of AdipoRon **22** were also successfully achieved (Fig. 10c). Mechanistic experiments and DFT calculations indicate a cooperative mechanism involving neighboring Pd centers. One Pd site anchors pivaldehyde and promotes its decarbonylation, releasing isobutane and generating surface-bound CO. In parallel, photoexcited electrons reduce an adjacent Pd centre, facilitating migration of the aryl group onto the adsorbed CO to form a crucial Pd-benzoyl species. Control experiments further support the importance of Pd-site proximity: at a fixed total metal loading, decreasing the Pd content while increasing the overall catalyst amount markedly lowers the yield of the target ketone and raises the amount of biphenyl byproduct, indicating the necessity of adjacent Pd sites for CO shuttling. Such spatial proximity of Pd atoms is therefore essential for efficient CO migration.

2.3 Redox-neutral coupling reaction

Redox-neutral cross-coupling reactions represent one of the most useful organic transformations in both academic and industrial communities. For example, the Nobel Prize-recognized Suzuki coupling, Negishi coupling and Heck coupling reactions have been widely employed in the construction of diverse drugs, natural products and functional materials. In contrast to oxidative or reductive couplings, the substrates are typically composed of a nucleophilic coupling partner and an electrophilic coupling partner. Thus, the external sacrificial oxidants or reductants are not required.

From 2019 to 2021, Wang and co-workers systematically developed a series of photocatalytic heterogeneous coupling reactions mediated by silver single-atom catalysts.[46–48] In their initial study, AgF was shown to undergo photolysis under visible light to generate a heterogeneous system containing atomically dispersed single-atom Ag(0) species (SAAg) together with Ag nanoparticles.[46] ESR (g = 2.003) analysis identifies SAAg as the catalytically active species (Fig. 11a). This system enables

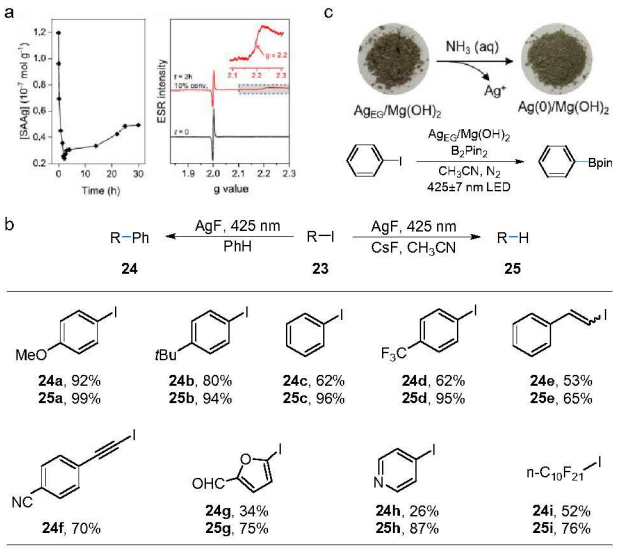

Fig. 11 (a) Variation of SAAg loading during the deiodination-phenylation. ESR spectral change of Ag(0)/AgI in the early stage of the photocatalytic reaction. Reproduced with permission.[46] Copyright 2019, American Chemical Society. (b) Selected examples of substrate scope. (c) Removal of Ag(I) to Ag(0) and the cross-coupling between aryl iodide and B_2Pin_2. Reproduced with permission.[47] Copyright 2021, Elsevier.

Green Chemistry Accepted Manuscript

This journal is © The Royal Society of Chemistry 20xx

selective dehalogenation/arylation of organic halides (**23**) with aromatic hydrocarbons, as well as hydrodehalogenation under mild conditions, without organic photocatalysts or additives. Substrate scopes encompassing C(sp), C(sp^2), and C(sp^3)–X bonds were demonstrated (Fig. 11b). Mechanistic studies support a radical pathway while excluding classical Ag(I)/Ag(III) oxidative insertion. Building on this concept, the group subsequently reported a plasmonic photocatalyst composed of Ag(0) single atoms supported on $Mg(OH)_2$ for the borylation of aryl and vinyl iodides.[47] Atomically dispersed Ag(0) species and Ag nanoparticles generated from partial reduction of AgCl enable efficient deiodination-borylation with boron reagents such as bis(pinacolato)diboron (Fig. 11c), exhibiting great functional group compatibility including halogens, nitrile, ester, aldehyde and ether, and applicability to sterically hindered, polycyclic, and heteroaryl substrates. Gram-scale synthesis under sunlight further highlights practical scalability. Subsequently, they further demonstrate that Ag(I) salts alone can mediate C–B coupling of aryl iodides with *in situ* formed Ag(0) single atoms.[48] Besides borylation with B_2pin_2, sulfenylation is also accessible with appropriate sulfur sources. Kinetic and spectroscopic studies indicate a "work-in-tandem" mechanism, in which Ag single atoms promote single-electron reduction of C–I bonds while Ag nanoparticles act as the visible-light absorber.

Visible-light-driven C–O coupling of aryl halides with alcohols has emerged as an attractive strategy for constructing aryl ethers under mild conditions. In 2020, Song and co-workers reported a heterogeneous C_3N_4–Ni/imidazole system capable of promoting C–O coupling of aryl halides with alcohols or water under visible light.[49] In this system, imidazole serves as an indispensable auxiliary ligand: the coupling yield plunges from 97% with 0.2 equivalents to merely 6% in its absence. DFT calculations further reveal that imidazole coordination elongates the Ni–N bond from 1.897 Å to approximately 1.944/1.981 Å, thereby creating a more accessible coordination environment at the Ni center and facilitating substrate binding. Primary alcohols such as EtOH, BnOH, and TFE afford aryl ethers

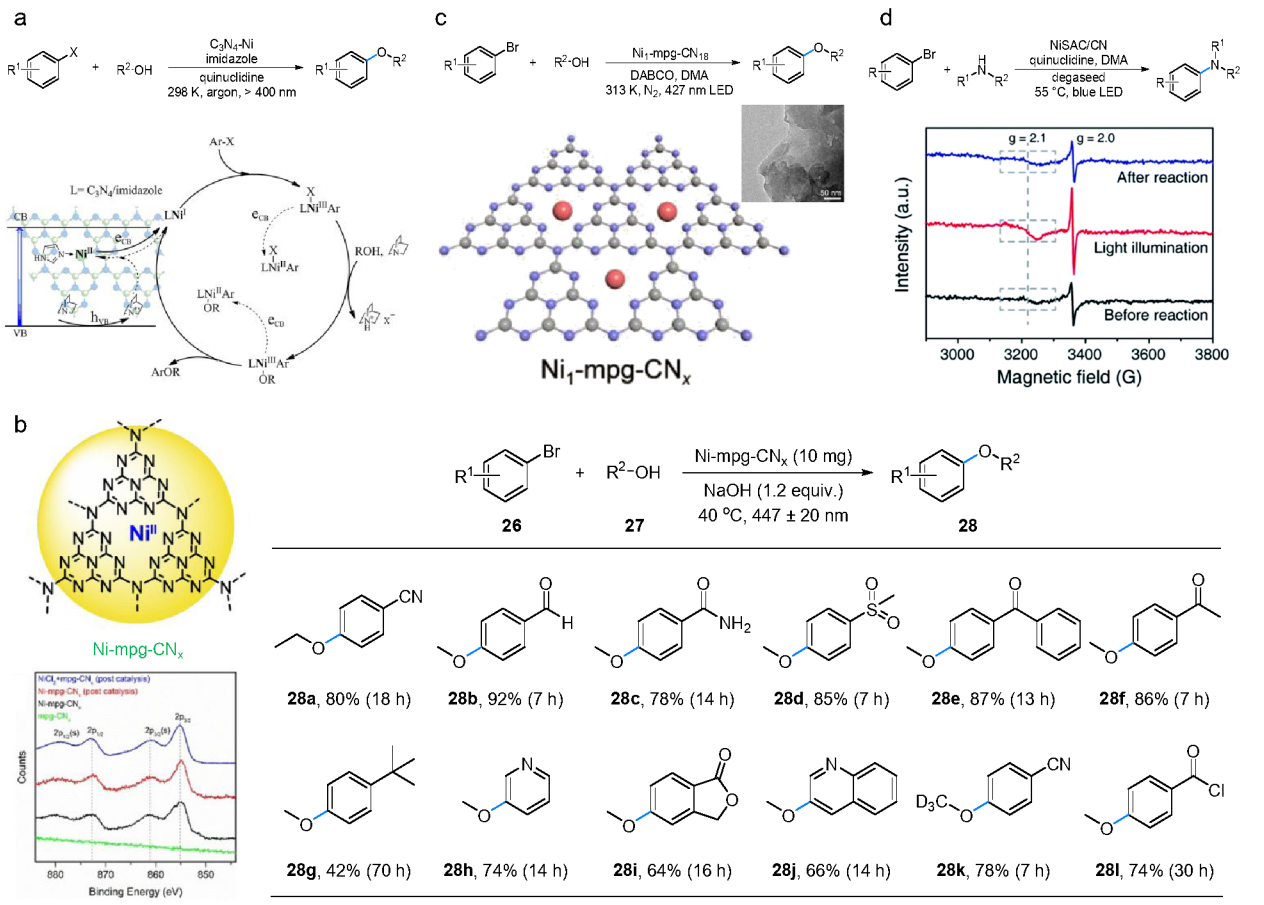

Fig. 12 (a) Schematic illustration of the C_3N_4–Ni/imidazole system for the C–O coupling of aryl halides with alcohols. Reproduced with permission.[49] Copyright 2020, American Chemical Society. (b) The structure and XPS analysis of Ni-mpg-CN$_x$ and selective examples of substrate scope for C–O coupling. Reproduced with permission.[50] Copyright 2021, John Wiley and Sons. (c) Schematic illustration of Ni single-atom mpg-CN system for the C–O coupling. Reproduced with permission.[51] Copyright 2023, John Wiley and Sons. (d) Schematic illustration of NiSAC/CN for C–N coupling reaction. Reproduced with permission.[52] Copyright 2022, The Royal Society of Chemistry.

Green Chemistry Accepted Manuscript

in 80-92% isolated yields within 12 h, while direct coupling with water delivered 4'-hydroxyacetophenone in 75% yield. In contrast, isopropanol and phenol show low reactivity (14-20%), and *t*ert-butanol or 2-furfuryl alcohol are unreactive. The catalyst can be reused for five cycles with > 96% selectivity, although longer irradiation is required due to gradual Ni loss. Spectroscopic studies confirm atomically dispersed Ni(II) species and efficient charge transfer from photoexcited CN to Ni sites and hole quenching by quinuclidine, which is essential for the catalytic cycle (Fig. 12a). Subsequently, the Reisner group applied similar Ni-deposited CN (Ni-mpg-CN_x) as an integrated heterogeneous photocatalyst for photocatalytic C–O coupling of aryl halides (**26**) with aliphatic alcohols (**27**).[50] The catalyst was prepared by microwave-assisted deposition of $NiCl_2$ onto mpg-CN_x, giving a total Ni loading of 4.14 ± 0.99 wt.% (Inductively coupled plasma optical emission spectroscopy, ICP-OES) and 2.2 wt.% of surface Ni (X-ray photoelectron spectroscopy, XPS), with no metallic Ni^0 detected. Under 447 nm irradiation at 40 °C with NaOH in alcohol solvent, electron-deficient aryl bromides afford aryl ethers in 78-92% isolated yields within 4-18 h (**28a-f**); aryl iodides reacted faster, while aryl chlorides require 60 °C to achieve full conversion. Primary alcohols (EtOH, *n*-PrOH, BnOH, MeOD) are competent, whereas tertiary alcohols are unreactive. The reactivity order C–I > C–Br > C–Cl correlates with C–X bond strength. Kinetic analysis (ΔH = 2.81 ± 0.31 kcal·mol^{-1}, $\Delta S^{\neq}$ = −70.0 ± 1 cal·mol^{-1}·K^{-1}) supports an associative oxidative-addition rate-limiting step,

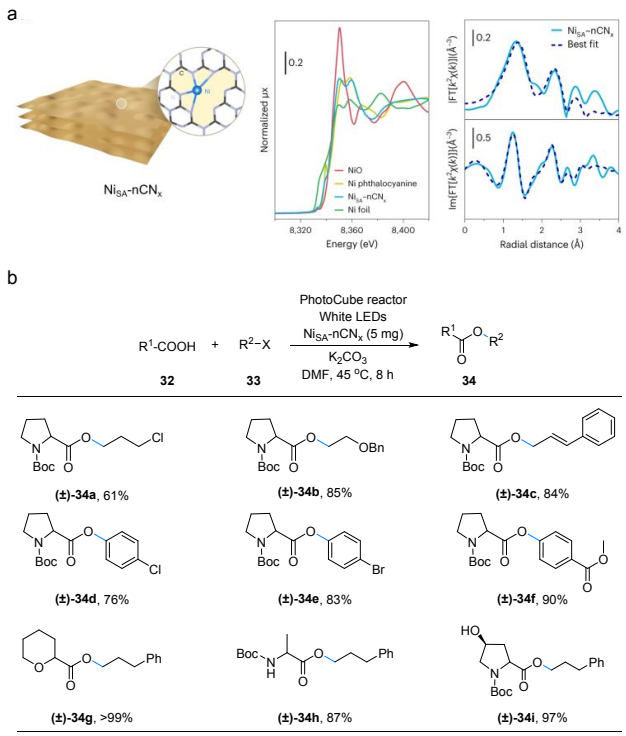

Fig. 13 (a) Schematic illustration of Ni$_{SA}$-nCN$_x$ and XAS spectra. Reproduced with permission.[53] Copyright 2023, Springer Nature. (b) Selective examples of substrate scope for C–O coupling of carboxylic acids and alkyl halides.

with Ni(I) species formed under photoexcitation and the alcohol quenches photogenerated holes to suppress recombination (Fig. 12b). Subsequently, a closely related Ni single-atom mpg-CN system reported by Chen and co-workers further corroborated the generality of this strategy, delivering aryl ethers in up to 99% yield from aryl bromides and primary alcohols under visible light (Fig. 12c).[51]

Despite the structural similarities among these Ni/CN catalysts, these three systems differ substantially in their requirements for additives and bases. Notably, their evolution reveals a progressive simplification of the catalytic design: while the earliest example relied on imidazole as an auxiliary ligand to regulate the coordination environment of the Ni center, later systems operate under ligand-free conditions. This shift from ligand-assisted to ligand-free catalysis represents a meaningful step toward more practical heterogeneous systems. However, while the proton-scavenging role of the base is generally recognized, the origin of the distinct base requirements across these systems (e.g., NaOH vs. DABCO) remains unclear, highlighting an unresolved aspect that merits further mechanistic investigation.

Moreover, Ni decorated CN can also been utilized in C–N coupling. In 2022, Yoo and co-workers reported an amination reaction of aryl bromides with Ni single atoms on CN (NiSAC/CN).[52] Under 427 nm Irradiation, ethyl 4-bromobenzoate and pyrrolidine give the C–N coupling product in 96% yield. *para*-substituted aryl bromides with CN, CO_2Et, CF_3, Ac groups result in 45-99% coupling yields, whereas electron-rich substrates (with OMe, Me) are less reactive (22-29%). Heteroaryl bromides and secondary cyclic amines (morpholine, piperidine, 1-acetylpiperazine) also demonstrate high reactivity. The catalyst was reused for three cycles without activity loss. Quasi *in situ* EPR shows reversible Ni^0 formation under light (g = 2.1), supporting a Ni(0)/Ni(II)/Ni(III)/Ni(I) photoredox cycle (Fig. 12d).

In 2023, Vilé and co-workers reported a photoredox-neutral C–O coupling of carboxylic acids (**32**) with alkyl or aryl halides (**33**) over Ni$_{SA}$-nCN$_x$.[53] The catalyst was prepared by impregnating $Ni(NO_3)_2{\cdot}6H_2O$ onto nanosheet CN followed by $NaBH_4$ reduction and microwave heating, and atomically dispersed Ni^{2+} centers are confirmed by X-ray absorption spectroscopy (XAS) and DFT (Fig. 13a). Under mild conditions (45 °C, white-light LED or solar irradiation) with K_2CO_3, ester products (**34**) are delivered in 10-97% yields across linear, benzylic, *α*-heteroatom-substituted and electron-deficient aryl halides (I > Br > Cl). Functional group tolerance encompasses ethers, esters, nitriles, alcohols, halogens and heterocycles; cyclic amino acid cores including *N*-Boc proline, alanine, azetidine, piperidine, indoline are particularly reactive (Fig. 13b). DFT calculation indicates carboxylic acid adsorption on Ni *via* its heterocyclic N atom, followed by Br^- abstraction and C–O bond formation. Recycling experiments show constant rate over four cycles with filtration reuse, and post-catalysis XAS reveals marginal structural change.

In the same year, Hyeon, Yoo and co-workers established an orthogonal dual photocatalytic system based on M_1/C_3N_4 (M = Pd, Ni).[54] Under visible light, photogenerated holes on CN drive

Green Chemistry Accepted Manuscript

This journal is © The Royal Society of Chemistry 20xx

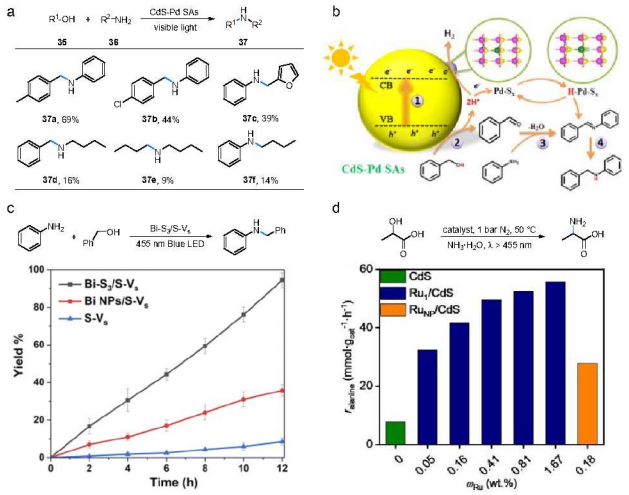

Fig. 14 (a) Selected examples of the substrate scope for CdS-Pd SAs photocatalyzed borrowing hydrogen reaction to access *N*-alkylamines. (b) The proposed mechanisms. Reproduced with permission.[55] Copyright 2022, American Chemical Society. (c) Schematic illustration of a $ZnIn_2S_4$-based dual-site photocatalyst for the *N*-alkylation of amines with alcohols. Reproduced with permission.[56] Copyright 2022, The Royal Society of Chemistry. (d) Schematic illustration of a Ru_1/CdS single-atom photocatalyst for the amination of α-hydroxy acids. Reproduced with permission.[57] Copyright 2024, John Wiley and Sons.

oxidative decarboxylative fluorination or aerobic alcohol oxidation, while the corresponding electrons are transferred to the metal sites, enabling Suzuki C–C coupling or Ni-catalyzed C–O bond formation. $Pd_1/C_3N_4/PPh_3$ efficiently couples aryl bromides bearing formyl, halogen, CF_3, alkyl, OMe or mesityl substituents and phenylboronic acid to biaryls in 67-99% yields. In parallel, Ni_1/C_3N_4 mediates a tandem process involving aerobic oxidation of 4-bromo-α-methylbenzyl alcohol followed by methoxylation, delivering 4'-methoxyacetophenone in 92% yield. Furthermore, a one-pot fluorination and Suzuki coupling affords fluorinated biaryl in 73% overall yield. The catalyst maintains activity over five consecutive runs without detectable Pd leaching.

Different from simple coupling process, hydrogen borrowing reactions have also been achieved. For instance, in 2022, Zou and co-workers developed a photocatalytic *N*-alkylation of amines with alcohols using CdS-Pd SAs (0.3 wt.% Pd).[55] With a 300 W Xe lamp ($\lambda > 420$ nm) at 25 °C, aniline and benzyl alcohol gave 100% conversion and 100% selectivity toward *N*-benzylaniline within 16 h, while a H_2 evolution at a rate of 11.8 mmol·gcat^{-1}·h^{-1} is inevitable. The protocol tolerates benzyl alcohol derivatives bearing Me, Cl or furfuryl substituents (**37a-c**), anilines with Me or Cl, and extends to aliphatic partners such as 1-butylamine and 1-butanol (Fig. 14a). Mechanistic studies indicate that photogenerated electrons are trapped at Pd–S_x sites and holes oxidize benzyl alcohol to aldehyde; subsequently, the Pd–S_x motif then acts as a hydrogen-autotransfer shuttle, enabling selective hydrogenation of the *in situ*-formed imine

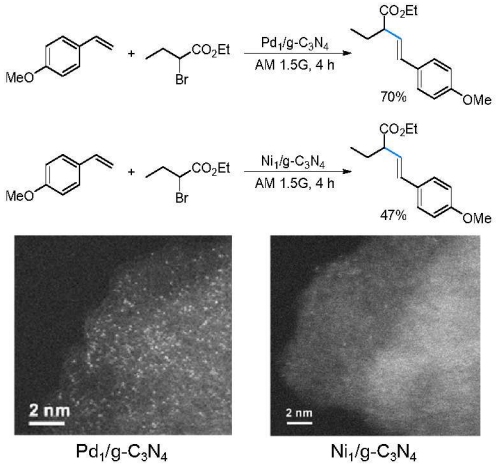

Fig. 15 Schematic illustration of photocatalytic Heck reaction. Reproduced with permission.[58] Copyright 2025, The Royal Society of Chemistry.

intermediate (Fig. 14b).

Another example by Mao group demonstrates a $ZnIn_2S_4$-based dual-site photocatalyst, Bi–S_3/S-V_s with a Bi loading of 0.89 wt.% for the *N*-alkylation of amines with alcohols.[56] Under irradiation with a 100 W blue LED at room temperature, the coupling of benzyl alcohol with aniline affords *N*-benzylaniline in 94.5% yield within 12 h without over-alkylation (Fig. 14c). The protocol tolerates 4-methyl- and *N*-methyl-aniline as well as methanol, giving secondary amines in 57-100% yields smoothly. Leveraging SACs for hydrogen borrowing transformations of biomass-derived hydroxy acids enables the direct synthesis of amino acids.[57] Chen and co-workers reported a Ru_1/CdS single-atom photocatalyst for the amination of α-hydroxy acids in aqueous NH_3 under visible light without external H_2 or high pressure. With lactic acid, Ru_1/CdS delivers a reaction rate of 41.6 mmol·g$_{cat}^{-1}$·h^{-1}, which is 1.7-fold higher than that of Ru_{NP}/CdS. The alanine formation rate is highly dependent on the Ru content (Fig. 14d). The substrate scope encompasses aliphatic and β-branched hydroxy acids, whereas 3-hydroxybutyric acid gives only trace amounts of the product. Catalyst recycling tests demonstrate that the activity is retained over four runs. Operando $^1H/^{13}C$ NMR indicates a Ru_1-mediated double-activation pathway, and DFT calculations reveal that the α-O–H bond dissociation energy decreases to 0.64 eV, compared to 0.78 eV and 1.17 eV for Ru_{NP}/CdS and CdS, respectively.

Recently, Zhang and co-workers prepared atomically dispersed $Pd_1/g\text{-}C_3N_4$ and $Ni_1/g\text{-}C_3N_4$ on CN nanosheets by freeze-electrochemical reduction for visible-light-driven oxidative Heck coupling.[58] Using 4-methoxystyrene and ethyl 2-bromobutyrate as starting materials, $Pd_1/g\text{-}C_3N_4$ gave a 70% yield in 4 h, significantly outperforming $Pd(PPh_3)_4$ (38%), whereas $Ni_1/g\text{-}C_3N_4$ delivered a 47% yield compared to 44% for $NiBr_2$·glyme (Fig. 15).

Green Chemistry Accepted Manuscript

Across the coupling reactions discussed above, a common mechanistic framework involves photogenerated holes driving substrate oxidation or dehydrogenation while electrons promote proton reduction or substrate reduction, with single-atom sites primarily modulating charge separation and SET pathways. However, several mechanistic ambiguities remain. The role of metal nuclearity is not yet unified: adjacent Pt single atoms and paired Pd sites are reported to be essential for C–H activation and CO migration, respectively, whereas isolated single-atom sites are sufficient for most reported reactions. Whether single-atom sites act as direct catalytic centers or solely as electronic modulators also varies across systems.

3. Addition reactions

Addition reactions of unsaturated hydrocarbons, particularly hydrogenation and difunctionalization of C=C and C≡C bonds, are cornerstone transformations in the petrochemical, fine chemical, and pharmaceutical industries.[59] Conventional hydrogenation typically relies on high-pressure H_2 and thermally driven metal catalysts, which raises safety, energy-consumption, and selectivity concerns.[60] In parallel, alkene functionalization offers atom-economic access to value-added molecules but often suffers from harsh conditions or limited catalyst recyclability.[61] Recent advances in photocatalysis and single-atom catalysis have provided new opportunities to address these challenges by enabling light-driven activation pathways, maximal metal utilization, and well-defined active sites. Here we have summarized the progress of single-atom photocatalytic hydrogenation, difunctionalization of alkenes, and CO_2 cycloaddition in sustainable organic synthesis (Fig. 16a).

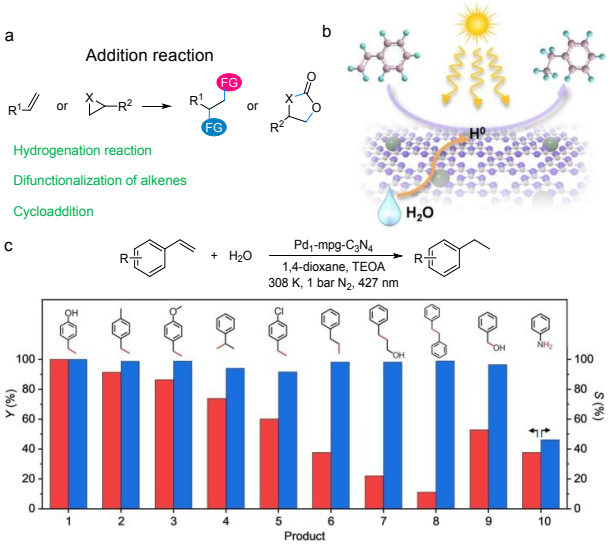

Fig. 16 (a) Representative addition reactions. (b) Schematic illustration of Pd_1-mpg-C_3N_4 for transfer hydrogenation using water. (c) The selected examples of the substrate scope. Reproduced with permission.[62] Copyright 2022, John Wiley and Sons.

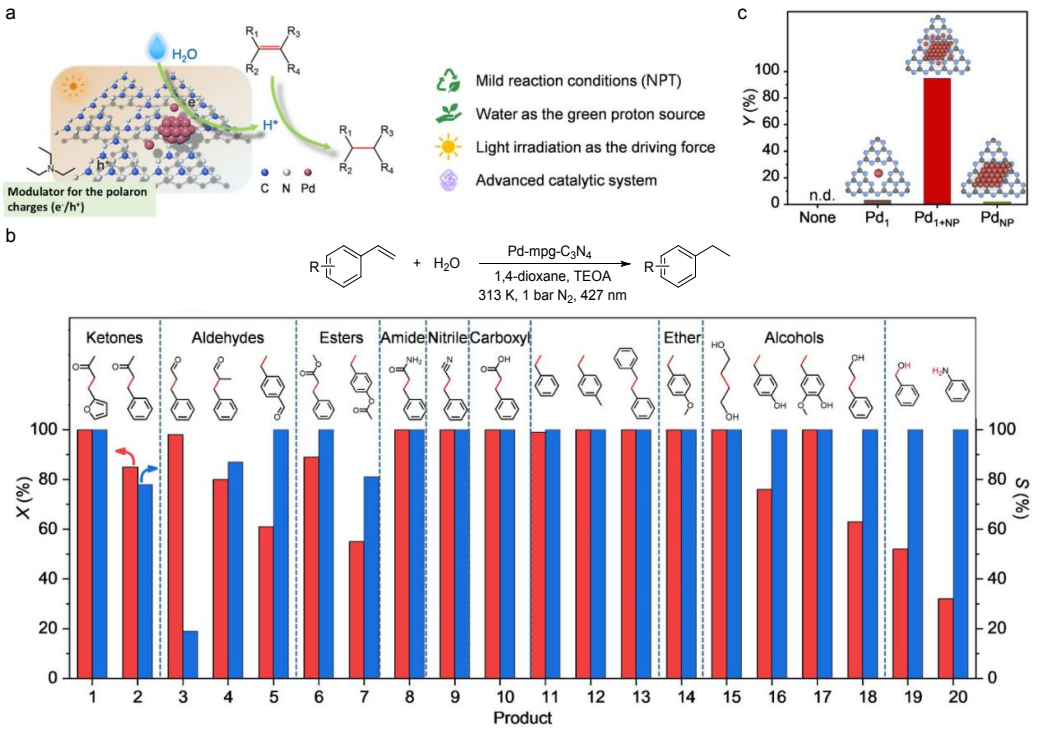

Green Chemistry Accepted Manuscript

This journal is © The Royal Society of Chemistry 20xx

Fig. 17 (a) Schematic illustration of Pd^0 nanoparticles and atomically dispersed Pd^{2+} and Pd^{4+} centers on CN for hydrogenation of alkenes. (b) Selected examples of the substrate scope. (c) Photocatalytic performance using chalcone as a substrate over different palladium configurations. Reproduced with permission.[63] Copyright 2025, John Wiley and Sons.

3.1 Hydrogenation reaction

Photocatalytic transfer hydrogenation using water as a proton source offers a greener alternative to high-pressure H_2 processes. In recent years, single-atom-photocatalyzed hydrogenation reactions have been notably reported by Chen and co-workers. In 2022, they developed a CN-supported Pd single-atom photocatalyst (Pd_1-mpg-C_3N_4) featuring Pd–N/C coordination for transfer hydrogenation using water as the hydrogen donor (Fig. 16b).[62] Upon 427 nm LED irradiation at 308 K and 1 bar N_2 in a mixture of water, 1,4-dioxane and triethanolamine (TEOA), styrene was converted to ethylbenzene in 90% yield with an apparent quantum efficiency (AQE) of 1.87% and a rate of 22.73 $mol_{ethylbenzene}$ $mol_{Pd}^{-1}\cdot h^{-1}$, which is 11-fold higher than that of a Pd-nanoparticle catalyst containing 0.49 wt.% Pd. The reaction tolerates styrenes bearing methyl, methoxy, hydroxy or chloro substituents as well as cinnamyl alcohol, internal alkenes such as 2-phenyl-1-propene and trans-stilbene. It also enables the reduction of benzaldehydes and nitrobenzenes to benzyl alcohols and anilines, whereas 1-decene remains unreactive (Fig. 16c).

Building on their previous work, in 2025, Chen and co-workers further developed a CN supported multivalent Pd catalyst containing 4.4 nm Pd^0 nanoparticles and atomically dispersed Pd^{2+} and Pd^{4+} centers (2.9 wt.% total Pd).[63] Under 427 nm LED irradiation, this catalyst enables rapid hydrogenation of C=C bonds to the corresponding saturated products within 4 h. Using chalcone as a representative substrate, this protocol achieves a 95% conversion to 1,3-diphenylpropan-1-one, while maintaining a high yield of 99% on a gram scale. (Fig. 17a, b). Control experiments reveal that neither Pd nanoparticles nor Pd single atoms alone are active (< 8% yield), highlighting the critical role of synergistic effect (Fig. 17c). The catalyst is recyclable for five cycles with slight activity loss. Operando EPR studies indicate efficient charge separation, where triethylamine modulates hole localization on Pd^{2+}, while Pd^0 nanoparticles reduce protons to hydrides that migrate to Pd single-atom sites to hydrogenate the bound substrate. Isotope labeling experiments with D_2O confirm water as the exclusive proton source.

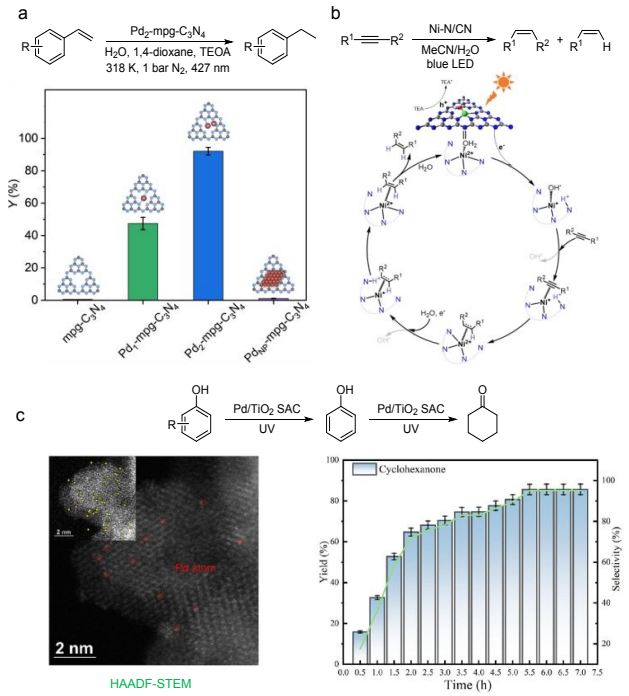

Fig. 18 (a) Catalytic performance of various catalysts for photocatalytic transfer hydrogenation. Reproduced with permission.[64] Copyright 2025, American Chemical Society. (b) The proposed mechanism for Ni–N/CN photocatalyzed semihydrogenation of alkynes under visible-light. Reproduced with permission.[65] Copyright 2023, John Wiley and Sons. (c) HAADF-STEM of Pd/TiO_2 single-atom catalyst and the photocatalytic performance of Pd/TiO_2 for reduction of 4-chlorophenol to cyclohexanone (green line indicates the yield). Reproduced with permission.[66] Copyright 2025, Elsevier.

In parallel, the same group proposed a CN-supported Pd diatomic catalyst (Pd_2-mpg-C_3N_4), prepared *via* a precursor-preselected wet-deposition strategy, in which Pd dimers were confirmed by aberration-corrected HAADF-STEM and automated atom-detection analysis.[64] Distinct from the multivalent system, Pd_2-mpg-C_3N_4 achieves efficient photocatalytic transfer hydrogenation through cooperative dual-atom sites, affording 4-ethylphenol in 92% yield from 4-vinylphenol, outperforming Pd single atoms of 47% and nanoparticles of 1% (Fig. 18a). The catalyst shows broad substrate versatility including olefins and biomass derivatives and maintains good recyclability. DFT calculations indicate that Pd dimers not only enhance substrate activation but also suppress the competing hydrogen evolution reaction compared to single-atom counterparts, underscoring the unique advantages of diatomic catalysts in selective and sustainable hydrogenation.

Besides olefins, single-atom catalytic semihydrogenation of alkyne using water as the hydrogen source has also been realized. In 2023, Zhao and co-workers reported a CN-supported single-atom nickel catalyst (Ni–N/CN) for semihydrogenation of alkynes under visible-light.[65] Atomically dispersed Ni^{2+} sites were formed by coordinating $NiCl_2$ to pyridinic nitrogen on CN nanosheets. The catalyst converts a series of terminal and internal alkynes bearing halogen, methoxy and alkyl groups to alkenes in 73-93% yields. Notably, excellent deuterium incorporation above 99% is achieved when D_2O is used, enabling the synthesis of deuterated alkenes such as methyl 4-(vinyl-d_3)benzoate. Mechanistic studies including EPR and DFT analyses show that visible light promotes the reduction of Ni^{2+} to Ni^+, coupled with water dissociation, and

Green Chemistry Accepted Manuscript

the resulting Ni^{+} species mediates proton transfer to the adsorbed alkyne to give alkenes (Fig. 18b).

To further extend water-driven hydrogenation to more complex cascade transformations, Jiang group recently reported a Pd/TiO_2 single-atom catalyst for the relay photocatalytic reduction of 4-chlorophenol to cyclohexanone.[66] The system achieves complete conversion with 86.14% yield and 95.63% selectivity for cyclohexanone production. Various

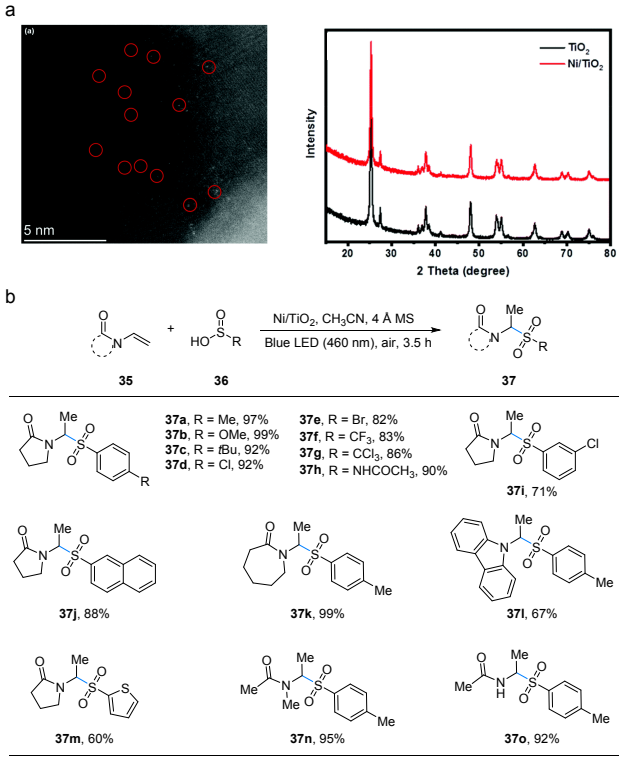

Fig. 19 (a) Characterization of Ni/TiO_2. Reproduced with permission.[67] Copyright 2021, The Royal Society of Chemistry. (b) Selected examples of substrate scope.

substituted phenols can be transformed to the corresponding cyclohexanones, where fluoro- and bromo-substituted substrates showed higher yields and selectivity, whereas methyl and methoxy gave negative results. Introduction of $AlCl_3$ can enhance cyclohexanone selectivity by suppressing over-reduction pathways (Fig. 18c).

3.2 Functionalization of alkenes

Beyond olefin hydrogenation, SACs have increasingly been applied to olefin difunctionalization to construct more complex scaffolds. For instance, in 2021, Wen and co-workers reported a Ni/TiO_2 single-atom photocatalyst containing 1.1 wt.% Ni for site-selective sulfonation of enamides (**35**) with sulfinic acids (**36**), affording *α*-amidosulfones (**37**) in 60-99% yields across 36 examples, with turnover number (TON) up to 18963.[67] In this protocol, the as prepared Ni/TiO_2 is characterized by aberration-corrected high resolution electron microscopy image, HAADF-STEM images and XPS patterns (Fig. 19a). The substrates are extended to alkyl, methoxy, halogen, acetamido, *ortho*-substituted arenes, naphthyl, thiophene, caprolactam, carbazole, acyclic enamides, and *N*-methyl or *N*-vinylacetamides (Fig. 19b). The *α*-position selectivity may be ascribed to the lone pair electrons of *N*, which can influence the electron density of the *α*-position of alkene. Gram-scale experiments maintain both high yield and TON, and the catalyst remains recyclable over five cycles, affording 84% yield with minimal Ni leaching (0.1-0.5 ppm).

Building on the versatility of SACs in enamide sulfonation, their application has been further extended to C–P bond formation. In 2024, Sun and co-workers developed a photoinduced ligand exchange (PILE) strategy to construct $Cu(I)–N_4$ single-atom sites on CN (Fig. 20a), which is applied in hydrophosphinylation of alkenes or alkynes (**38**) with diphenylphosphine oxides (**39**), using 390 nm LED at room temperature without additives.[68] The system delivers a high TOF of 1507 h^{-1} with up to 98% yield at 1 mmol scale and 94% yield at 10 mmol scale. The protocol tolerates various alkenes bearing cyano (**40a**), trimethylsilyl (**40b**), hydroxyl (**40c**), halogen, carbonyl, heteroaryl groups, cyclic olefins (**40d**-**e**), as well as terminal alkynes (**40j**-**m**), affording *Z*-alkenylphosphine oxides with Z/*E* ratios up to 96:4, this outperforming selectivity maybe owing to π-π stacking or the electronic effect of Cu_1/CN (Fig. 20b). The catalyst can be recycled for seven cycles, retaining outstanding activity with yields of up to 85%. Finally, the reaction is initiated by single-electron oxidative addition of a carbon-centered radical to Cu(I) with a low activation barrier of 1.5 kcal·mol^{-1}.

3.3 CO_2 Cycloaddition

CO_2, a well-studied C1 substrate in single-atom photocatalytic energy-conversion applications has also been applied to

Green Chemistry Accepted Manuscript

This journal is © The Royal Society of Chemistry 20xx

Please do not adjust margins

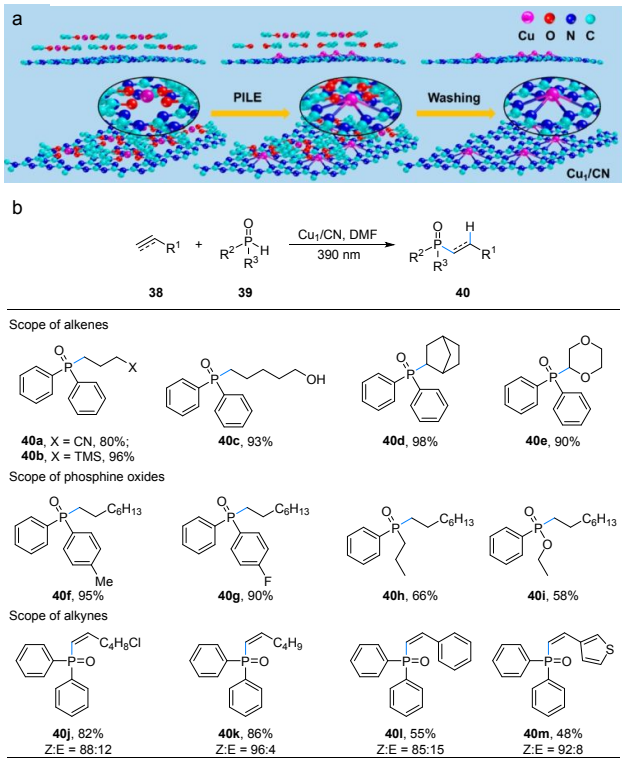

Fig. 20 (a) Synthesis and structure of the Cu_1/CN catalyst. Reproduced with permission.[68] Copyright 2024, American Chemical Society. (b) Selected examples of substrate scope.

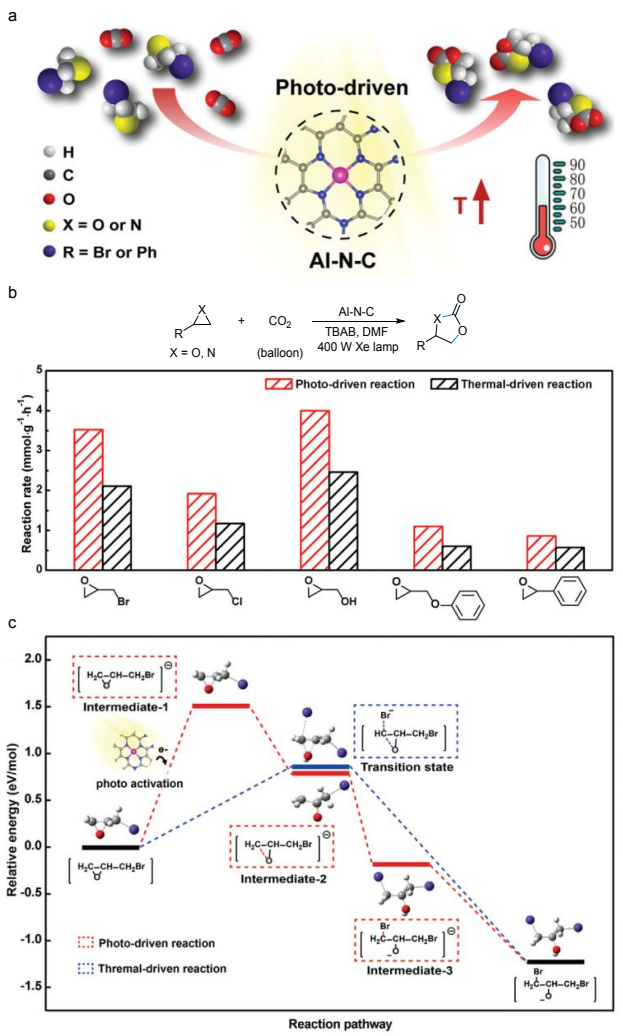

Fig. 21 (a) Schematic illustration of the single-atom catalyst Al–N–C for photocatalytic CO_2 cycloaddition with epoxides. (b) Selected examples of the substrate scope. (c) DFT calculation for the rate-limiting step. Reproduced with permission.[69] Copyright 2021, John Wiley and Sons.

cycloaddition reactions. In 2021, Chen and co-workers reported a molecule-confined pyrolysis strategy to prepare porous carbon nanosheets containing atomically dispersed Al–N_4 sites with a high loading of 14.4 wt.%.[69] Under full-spectrum irradiation (400 mW cm^{-2}), the SAC Al–N–C efficiently converts CO_2 and epoxides to cyclic carbonates, affording about 95% yields and a reaction rate of 3.52 $mmol \cdot g^{-1} \cdot h^{-1}$, which is approximately 1.7-fold higher than that of the thermal-only reaction at 62 °C (Fig. 21a). The substrate scope includes terminal epoxides bearing Br, Cl, OH, phenoxy or aziridine functionalities, which are smoothly transformed into the corresponding products, whereas more sterically hindered substrates such as 2-(phenoxymethyl)-oxirane and styrene oxide exhibit lower reactivity (Fig. 21b). The catalyst maintains its performance over five consecutive cycles with negligible

Green Chemistry Accepted Manuscript

morphological changes. Operando EPR, ultraviolet photoelectron spectroscopy (UPS) and DFT calculations reveal that photogenerated electrons are transferred from the Al–N–C conduction band to the epoxide, generating a negatively charged intermediate that obviates the additional energy required for ring-opening under thermal conditions. The electron subsequently returns to the catalyst, completing a light-enhanced Lewis acid-base (Al and N sites) catalytic cycle (Fig. 21c).

Across the addition reactions discussed above, single-atom sites play diverse yet complementary roles in managing photogenerated charge carriers and facilitating key elementary steps, such as electron trapping and hydrogen transfer, while photogenerated holes can participate in substrate or water oxidation. The influence of metal nuclearity, as highlighted in Section 2, is particularly evident in transfer hydrogenation, where Pd dimers and mixed-valence Pd systems can outperform both isolated Pd single atoms and Pd nanoparticles. Furthermore, Pd- and Ni-based systems can follow distinct hydrogen-transfer pathways even when water serves as the hydrogen source, underscoring how strongly reaction mechanisms depend on the identity, nuclearity, and coordination environment of the active sites. Establishing a general framework linking these structural features to the preferred hydrogen-transfer pathways therefore remains an important challenge for the rational design of single-atom photocatalysts.

4. Functional group oxidations

Functional group oxidation represents one of the most fundamental and synthetically enabling transformations in organic synthesis, as it converts a specific moiety of a substrate into a higher oxidation state and enhanced derivatization capability, providing versatile “synthetic handles” for downstream bond construction and molecular diversification. Conventional oxidation protocols, however, typically rely on stoichiometric oxidants, harsh conditions, or precious-metal complexes, which intrinsically constrain safety, atom economy, and selectivity control.[70] The introduction of single-atom photocatalysis offers a new design perspective to these classic transformations: On the one hand, isolated metal sites can serve as efficient “electron/hole pumps”, accelerating the separation and directional transfer of photogenerated charge carriers in semiconductors. On the other hand, the precisely tunable local coordination environment enables the selective adsorption and activation of both substrates and oxidants, steering the formation of specific ROS such as $\cdot O_2^-$, surface-bound ·OH, or mild peroxo intermediates.[71] This capability effectively reframes the long-standing trade-off between strong oxidative activity and over-oxidation as a controllable challenge of selectivity.[72] Moreover, the discrete electronic structures and engineerable coordination environments of single-atom sites impart near-molecular-level uniformity and tunability in liquid-phase reactions, while preserving the practical advantages of heterogeneous catalysis, including facile separation, recyclability, and minimal metal leaching.[20] Across diverse reaction types such as aromatic/aliphatic C–H oxidation, selective oxidation of alcohols/aldehydes, dehydrogenation, and the upgrading of biomass-derived platform molecules, a growing body of representative studies collectively underscores the distinctive ability of single-atom photocatalysts to simultaneously enhance both activity and selectivity (Fig. 22a).

4.1 Oxidation of aromatics

In 2020, Fu and co-workers designed a copper single-atom-decorated tubular CN photocatalyst (SA-Cu-TCN) for the oxidation of aromatics.[73] By intercalating sodium copper chlorophyllin into a supramolecular precursor followed by thermal treatment, Cu atoms were cooperatively anchored in two coordination motifs: $Cu–N_3$ (in-plane) and $Cu–N_4$ (interlayer), which concurrently established in-plane and interlayer charge-transport channels, therefore, significantly enhancing charge separation and mobility. Leveraging this architecture, SA-Cu-TCN enables highly selective visible-light-driven oxidation of benzene to phenol: under mild conditions, efficient activation of oxidants (e.g., H_2O_2) by photogenerated holes delivers 92.3% benzene conversion with 99.9% phenol selectivity, while effectively suppressing over-oxidation to undesired by-products (Fig. 22b). Notably, the recovered catalyst retains its crystalline structure after reaction, underscoring its excellent structural robustness.

4.2 Oxidation of alcohols

As a pivotal precursor to a diverse array of functional groups (e.g., aldehydes, ketones, and carboxylic acids), the selective oxidation of

Green Chemistry Accepted Manuscript

This journal is © The Royal Society of Chemistry 20xx

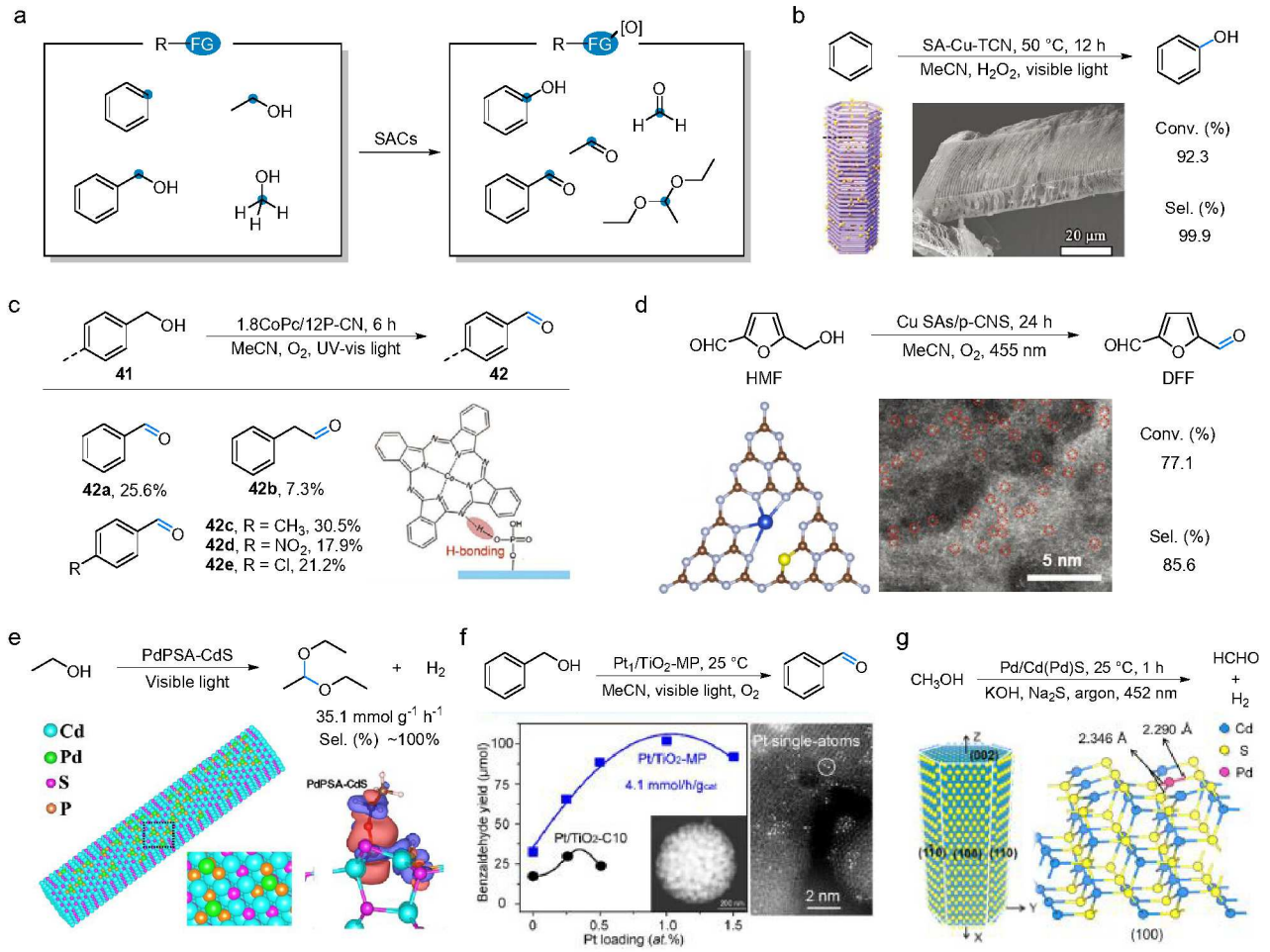

Fig. 22 (a) Representative SAC promoted photo oxidation reactions. (b) Schematic illustration of SA-Cu-TCN for the oxidation of aromatics. Reproduced with permission.[60] Copyright 2020, John Wiley and Sons. (c) Schematic illustration of CoPc/P-CN for the oxidation of benzyl alcohols. 1.8CoPc/12P-CN indicates a 1.8% mass ratio of CoPc to CN, a 12% mass ratio of NaH_2PO_4 to CN. Reproduced with permission.[61] Copyright 2020, John Wiley and Sons. (d) Biomass valorization with Cu SAs/p-CNS. Reproduced with permission.[62] Copyright 2021, John Wiley and Sons. (e) Schematic illustration of PdPSA-CdS for selective ethanol oxidation. Reproduced with permission.[63] Copyright 2021, Elsevier. (f) Schematic illustration of Pt_1/TiO_2-MP for oxidation of benzyl alcohol to benzaldehyde. Reproduced with permission.[64] Copyright 2022, Elsevier. (g) Schematic illustration of Pd_1 + Pd cluster/CdS for oxidant-free methanol dehydrogenation. Reproduced with permission.[65] Copyright 2024, American Chemical Society.

alcohols has garnered significant attention in the field of single-atom photocatalysis. In 2020, Jing and co-workers reported a phosphate-modulated ultrathin Co phthalocyanine and CN heterojunction photocatalyst (CoPc/P-CN) featuring exposed Co–N_4(II) single-atom sites for oxidation of benzyl alcohols (Fig. 22c).[74] The introduction of phosphate groups increases surface hydroxyl density and hydrogen-bonding interactions, suppresses π-π stacking of CoPc, and yields an ultrathin (near 4 nm) two-dimensional heterojunction. This architecture promotes efficient electron transfer from CN to CoPc and subsequently to Co–N_4 active sites, enhancing O_2 adsorption and activation. Benzyl alcohols (**41**) are selectively oxidized to aromatic aldehydes (**42**) under O_2 at ambient pressure. Substrates bearing electron-withdrawing groups such as nitro and chloro are well tolerated with side reactions effectively suppressed. Although recycling experiments for the alcohol oxidation reaction were not reported in the original study, the structural stability of the CoPc/P-CN heterojunction was demonstrated in a parallel photocatalytic system, where 0.5CoPc/9P-CN maintained its activity over five consecutive cycles during 2,4-dichlorophenol degradation. This result suggests that the hydrogen-bonding interaction provide sufficient interfacial stability to maintain the CoPc/P-CN architecture under photocatalytic conditions.

In the context of biomass valorization, Li and co-workers fabricated a CN catalyst co-modified with Cu single atoms and S dopants (Cu SAs/p-CNS) in 2021.[75] In this system, Cu single atoms serve as electron-trapping centers while S sites act as hole-accumulation regions, enabling efficient charge separation. Under visible light at room temperature with O_2, the catalyst selectively oxidizes 5-hydroxymethylfurfural (HMF) to 2,5-diformylfuran (DFF), achieving 77.1% conversion and 85.6% selectivity (Fig. 22d). Mechanistic studies show that Cu–N_4 sites

Green Chemistry Accepted Manuscript

activate O_2 to generate $\cdot O_2^-$, while holes at S-rich regions drive alcohol dehydrogenation and stepwise oxidation *via* alkoxy-radical intermediates. The H_2O_2 by-product is subsequently consumed by photogenerated holes, thereby suppressing DFF overoxidation while simultaneously sustaining the oxidative catalytic cycle.

At the same time, Guo and co-workers developed a CdS nanorod photocatalyst incorporating partially reduced Pd single atoms coordinated with phosphorus (PdPSA-CdS) for selective ethanol oxidation.[76] The Pd–P_3 sites create a cooperative redox interface, wherein photogenerated electrons localizing on Pd and holes on adjacent P sites, promoting alcohol dehydrogenation. Under visible-light irradiation above 420 nm, ethanol is converted *via* acetaldehyde to 1,1-diethoxyethane (DEE) with H_2 evolution, achieving a reaction rate of 35.1 $mmol \cdot g^{-1} \cdot h^{-1}$, near-quantitative DEE selectivity, and an apparent quantum yield (AQY) of 2.15% (Fig. 22e). Notably, this performance significantly surpasses that of Pd nanoparticles and S-coordinated Pd single-atom analogues.

Subsequently, Kuai and co-workers designed a mesoporous TiO_2 photocatalyst with high-loading Pt single atoms (Pt_1/TiO_2-MP) for oxidation of benzyl alcohol to benzaldehyde at 25 °C under 1 atm O_2 (Fig. 22f).[77] The catalyst delivers a benzaldehyde formation rate of 4.1 $mmol \cdot h^{-1} \cdot g^{-1}$ with near-quantitative selectivity, which is further increased to 4.5 $mmol \cdot h^{-1} \cdot g^{-1}$ upon

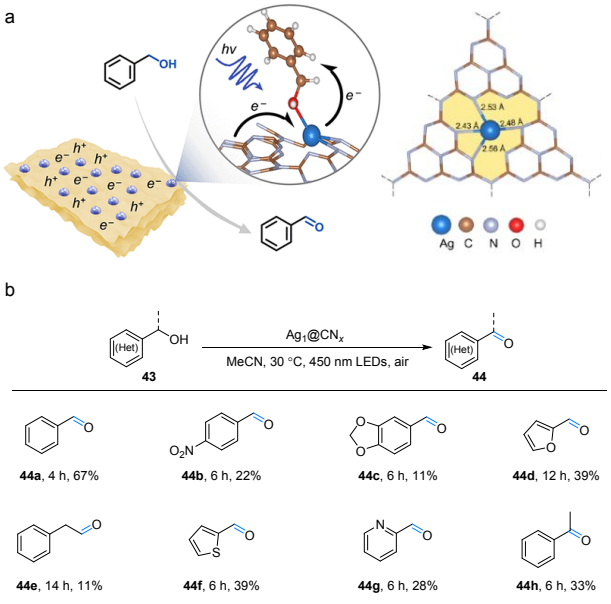

Fig. 23 (a) Schematic illustration of $Ag_1@CN_x$ for benzyl alcohol oxidation. Reproduced with permission.[79] Copyright 2025, American Chemical Society. (b) Selected examples of substrate scope.

incorporation of trace Au nanoparticles, owing to plasmon-enhanced absorption and hot-electron injection.

As the simplest and smallest alcohol, methanol oxidation/dehydrogenation plays a central role in fuel and energy chemistry and has recently attracted increasing interest in single-atom photocatalysis. In 2024, Wang and co-workers developed a CdS photocatalyst containing both Pd single atoms and Pd clusters (Pd_1 + Pd cluster/CdS) *via* sequential ion-exchange and photodeposition for oxidant-free methanol dehydrogenation.[78] Under 452 nm visible-light irradiation at room temperature in an inert atmosphere, methanol is selectively converted to formaldehyde with concurrent H_2 evolution without external oxidants or sacrificial agents (Fig. 22g). Mechanistic studies revealed a Janus-type function: Pd_1 sites trap holes and oxidize methanol *via* C–H cleavage to generate $\cdot CH_2OH$ intermediates, while Pd clusters reduce protons to H_2, suppressing electron-hole recombination. With the addition of KOH and Na_2S, the system achieves a Pd-based TOF of 1.14 s^{-1} and AQYs of 87 ± 1% for both H_2 and formaldehyde, representing one of the most efficient photocatalytic alcohol-dehydrogenation systems.

In 2025, Vilé employed an Ag single-atom-modified CN photocatalyst ($Ag_1@CN_x$) for benzyl alcohol oxidation with a TON of 1098 $mmol_{prod} \cdot mmolAg^{-1}$.[79] The incorporation of Ag single atoms prolongs the excited-state lifetime of CN, sustaining charge-separated states that promote surface redox chemistry. Full conversion of benzyl alcohol is achieved within 60 min (Fig. 23a). The protocol tolerates both electron-donating and electron-withdrawing substituents, and can be extended to heteroaromatic substrates such as furan (**44d**), thiophene (**44f**) and pyridine (**44g**), enabling the efficient oxidation of aliphatic alcohols to the corresponding aldehydes (Fig. 23b).

4.3 Oxidation of aldehydes

Beyond alcohols, the selective oxidation of aldehydes has also been explored within single-atom photocatalytic systems. In 2021, Huang and co-workers investigated the size effect of Pt species on CN, showing that Pt single atoms outperform nanoclusters and nanoparticles in capturing and separating charge carriers.[80] Building on this insight, they developed a photocatalytic system for aromatic aldehyde oxidation coupled with hydrogen evolution. Using benzaldehyde as a model substrate, selective oxidation to benzoic acid proceeds in aqueous media without external oxidants (Fig. 24a). Mechanistic studies reveal that Pt single atoms preferentially capture and shuttle holes, accelerating aldehyde oxidation and enhancing electron availability for H_2 evolution. In contrast, larger Pt particles trap both electrons and holes, leading to enhanced recombination and diminished catalytic efficiency.

In 2024, Hou and co-workers developed a high-loading Fe single-atom photocatalyst on CN with quasi-five-coordinated Fe–N_x sites for the selective oxidation of glucose to gluconic acid.[81] Using peroxymonosulfate as oxidant under simulated sunlight, 36.3% glucose conversion and 91.6% selectivity are achieved within 30 min. Calculation results indicate the strong electron transfer from Fe_1CN-20 (20 means mass percentage of iron element added initially) to both peroxymonosulfate and

Green Chemistry Accepted Manuscript

This journal is © The Royal Society of Chemistry 20xx

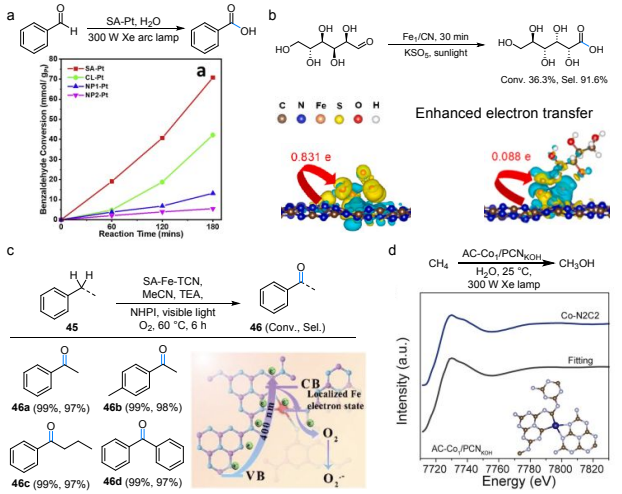

Fig. 24 (a) Photocatalytic performance of single-atom Pt, Pt cluster and Pt nanoparticle for aldehyde oxidation coupled with hydrogen evolution. Reproduced with permission.[80] Copyright 2021, Elsevier. (b) Schematic illustration of Fe single-atom photocatalyst for the selective oxidation of glucose to gluconic acid. Reproduced with permission.[81] Copyright 2024, Elsevier. (c) Selected examples of Fe–N_4 sites catalyzed selective oxidation of aliphatic C(sp^3)–H bonds. Reproduced with permission.[82] Copyright 2022, John Wiley and Sons. (d) Schematic illustration of asymmetric Co–C_2N_2 coordination environment. Reproduced with permission.[83] Copyright 2023, Elsevier.

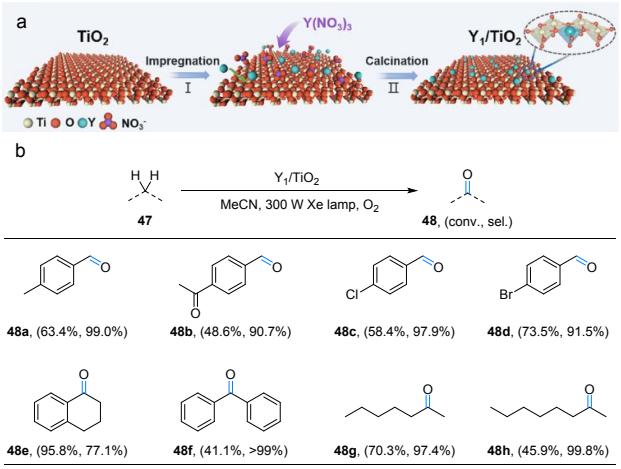

Fig. 25 (a) Schematic illustration of the preparation of single-Yttrium atom catalyst. Reproduced with permission.[84] Copyright 2024, American Chemical Society. (b) Selected examples of the substrate scope for benzylic C(sp^3)–H oxidation.

glucose molecules (Fig. 24b). In this system, singlet oxygen serves as the dominant reactive species, supplemented by holes, superoxide, and hydroxyl radicals (h^+, $\cdot O_2^-$, and ·OH), suppressing C–C cleavage and over-oxidation, demonstrating the capability of single-atom catalysis to regulate ROS and enhance selectivity.

4.4 Oxidation of C–H bonds

Compared with the oxidation of oxygen-containing functional groups, the selective oxidation of aliphatic C(sp^3)–H bonds remains intrinsically challenging due to their high bond dissociation energies, low polarity, and the absence of directing groups. To address these challenges, Fu and co-workers developed a tubular CN photocatalyst in 2022, featuring atomically dispersed Fe sites in a low-spin Fe(II)–N_4 coordination environment for selective oxidation of aliphatic C(sp^3)–H bonds.[82] The Fe–N_4 sites facilitate O_2 adsorption and electron transfer to generate superoxide radicals. Under visible light with 1 atm O_2 at approximately 60 °C, ethylbenzene is selectively oxidized to acetophenone (**46a**) with 99% conversion and 99% selectivity (Fig. 24c). Radical trapping, EPR and DFT calculations support a superoxide-dominated pathway, which avoids the nonselective reactions associated with ·OH. Moreover, this strategy is further extended to other benzylic C–H substrates.

In addition, even ·OH, which is often considered challenging to control, can be harnessed for selective C(sp^3)–H oxidation when its generation is kinetically regulated. In 2023, Zhai and co-workers reported an asymmetrically coordinated cobalt single-atom site on CN for methane oxidation.[83] By transforming the coordination environment from Co–N_4 to asymmetric Co–C_2N_2 (AC-Co_1/PCN_{KOH}), the Co center adopts a lower oxidation state with moderate hole enrichment, regulating the electron required for water oxidation (Fig. 24d). This modulation suppresses multi-electron oxygen evolution and instead favors a single-electron water oxidation pathway, leading to the generation of surface-bound hydroxyl radical intermediates. Thus, with water as the sole oxygen source, methane is selectively oxidized to methanol with 87.22% selectivity while suppressing over-oxidation to CO_2 and formic acid.

Thereafter, Duan and co-workers investigated a rare-earth single-atom photocatalyst based on Yttrium sites supported on TiO_2 for benzylic C(sp^3)–H oxidation. The catalyst features a $Y_1^{\delta+}$–O–Ti^{3+} motif that induces oxygen vacancies and improves charge separation (Fig. 25a).[84] With toluene as the substrate under Xe lamp at room temperature, benzaldehyde is obtained with 94.1% selectivity while suppressing over-oxidation to benzoic acid or CO_2. The method is applicable to a wide range of alkyl-substituted arenes and selected aliphatic substrates, including 1,2,3,4-tetrahydronaphthalene (**48e**, 95.8% conv., 77.1% sel.), diphenylmethane (**48f**, 41.1% conv., > 99% sel.), heptane (**48g**, 70.3% conv., 97.4% sel.) and octane (**48h**, 45.9% conv., 99.8% sel.), even though in some cases, the conversion and selectivity are limited (Fig. 25b). Mechanistic studies indicate that photogenerated holes promote the formation of benzyl radicals, whereas electrons reduce O_2 to $\cdot O_2^-$, and lattice oxygen cooperates with molecular oxygen to achieve selective oxidation.

Building on these advances, Li and co-workers in 2025 explored a low-coordination single-atom catalyst featuring Pd–Bi interactions (Pd–O_3/Bi_2WO_6).[85] The tailored coordination environment enhances hole trapping, prolongs charge-carrier lifetimes, and weakens

Green Chemistry Accepted Manuscript

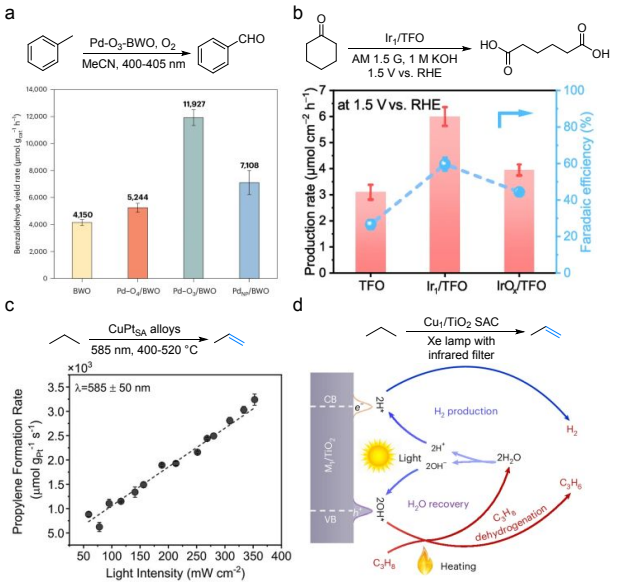

Fig. 26 (a) Photocatalytic performance of Pd–O_3/Bi_2WO_6 for the selective oxidation of toluene to benzaldehyde. Reproduced with permission.[85] Copyright 2025, Springer Nature. (b) PEC cyclohexanone oxidation performance over TFO, Ir_1/TFO and IrO_x/TFO photoanodes. Reproduced with permission.[86] Copyright 2025, Springer Nature. (c) Power-dependent study of $CuPt_{SA}$ starts disentangling between photothermal and nonthermal effects in plasmonic propane dehydrogenation. Reproduced with permission.[87] Copyright 2025, American Chemical Society. (d) Mechanisms for Cu_1/TiO_2 photo-thermal catalytic propane dehydrogenation. Reproduced with permission.[88] Copyright 2025, Springer Nature.

product adsorption. Under visible light with O_2 as the terminal oxidant, the system enables selective oxidation of toluene to benzaldehyde, achieving 95% conversion and 95% selectivity with a benzaldehyde formation rate of 11927 μmol·g^{-1}·h^{-1} (Fig. 26a). Notably, the reaction is further demonstrated in a continuous-flow photoreactor, delivering a space-time yield of 5.1 kg·m^{-3}·h^{-1}. With mechanistic investigation, a hole-initiated radical pathway is supported, in which Pd–O_3 sites promote C–H activation while suppressing the over-oxidation of benzaldehyde.

Beyond photocatalytic systems, photoelectrocatalytic (PEC) approaches provide additional control through applied bias and interfacial engineering. In 2025, Xiong and co-workers developed a Ti-doped α-Fe_2O_3 (TFO) photoanode decorated with Ir single atoms (Ir_1/Ti-α-Fe_2O_3), where Ir adopts an Ir–O_5 coordination environment that improves hole utilization while suppressing competing water oxidation.[86] The system enables selective ring-opening oxidation of cyclohexanone to adipic acid using water as the sole oxygen source. In alkaline electrolyte under simulated sunlight with an applied bias of 1.5 V vs. the reversible hydrogen electrode (RHE), the reaction achieved an adipic acid formation rate of 6.0 μmol·cm^{-2}·h^{-1}, a Faradaic efficiency of approximately 60% and a selectivity of 88%, outperforming both unmodified or IrO_x-modified counterparts (Fig. 26b). Operando spectroscopic and isotope-labeling studies indicate a hole-driven adsorbed ·OH transfer pathway, rather than a free ·OH oxidation mechanism. Furthermore, coupling with an amorphous silicon photocathode enables an unbiased PEC device that sustains adipic acid production for over 80 h.

Finally, beyond oxygen-involving oxidation reactions, single-atom motifs also offer unique advantages in the C–H activation and dehydrogenation of inert alkanes. In 2025, Swearer and co-workers reported dilute CuPt plasmonic single-atom alloys, demonstrating that Pt single atoms can remain stable under propane dehydrogenation (PDH) conditions at elevated temperatures (400-520 °C) while preserving the Cu localized surface plasmon resonance (LSPR).[87] Under 585 nm illumination, plasmon excitation induces transient atomic-scale localization of non-thermal holes, generating a short-lived yet highly oxidative species that significantly lowers the apparent activation barrier for the initial C–H bond scission in propane (from near 99 to 68 kJ·mol^{-1}), thereby increasing propylene formation while suppressing deep dehydrogenation and coking (Fig. 26c). In parallel, Liu, Zhang and co-workers developed a Cu_1/TiO_2 photo-thermal platform that enables selective PDH with water as the reaction medium.[88] In photocatalytic condition, water activation on TiO_2 generates surface-bound ·OH species that abstract hydrogen from propane at adjacent Cu single-atom sites with a low barrier, forming stably adsorbed propyl radicals that dehydrogenate to propylene while avoiding O_2-driven over-oxidation (Fig. 26d). The strategy is also applied to ethane and butane and operates under natural sunlight at temperatures as low as 10 °C, highlighting a compelling route for directly coupling solar energy input with energy-intensive industrial dehydrogenation processes.

Across the oxidation reactions discussed above, a recurring mechanistic feature is the ability of single-atom sites to regulate photogenerated charge carriers and facilitate oxidant activation and ROS generation, with substrate oxidation subsequently driven by photogenerated holes and/or the resulting ROS. However, the dominant oxidative pathway varies widely across systems: superoxide radicals dominate in Fe–N_4-catalyzed ethylbenzene oxidation, whereas surface-bound ·OH are proposed for Co–C_2N_2-mediated methane oxidation. Whether single-atom sites directly activate C–H bonds or primarily act as electron-transfer centers also remains debated, with different systems invoking direct C–H activation or indirect reactive-species-mediated pathways. Moreover, the factors governing the balance between selective oxidation and overoxidation and product selectivity, such as metal coordination, support properties and reactive-species lifetime, are not yet fully understood. A unified picture of how coordination environments control generation and selectivity of ROS is still lacking.

5. Other reactions

Besides conventional coupling, addition and oxidation reactions, single-atom photo- and photoelectrocatalysis have also exhibited unique advantages in selective C–C bond cleavage of biomass-derived substrates or halogen-radical-mediated C–H functionalization. In 2023, Wang and Tang

Green Chemistry Accepted Manuscript

This journal is © The Royal Society of Chemistry 20xx

reported a Ni/TiO_2 photocatalyst where Ni^{2+} single atoms are anchored in a Ni–O_5

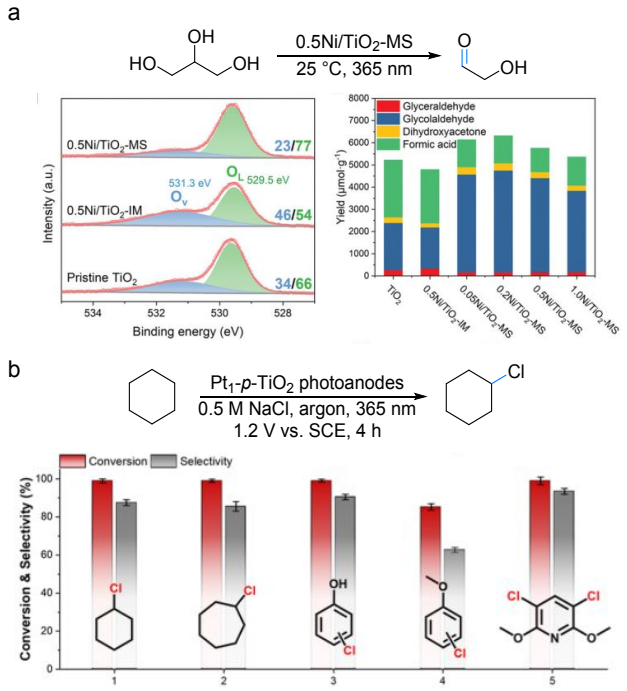

Fig. 27 (a) High-resolution O 1s XPS spectra and photocatalytic performance of Ni/TiO_2 photocatalysts for selective C–C bond cleavage of biomass-derived substrates. Reproduced with permission.[89] Copyright 2023, John Wiley and Sons. (b) Selected examples for the C–H chlorination reaction. Reproduced with permission.[90] Copyright 2025, American Chemical Society.

coordination environment *via* a molten-salt (MS) method, creating vacant energy levels near the TiO_2 conduction band. High-resolution O 1s XPS spectra show that 0.5Ni/TiO_2-MS features lowest content of oxygen vacancies (oxygen vacancy/lattice oxygen ratio = 23/77).[89] These sites act as electron sinks and oxygen adsorption centers, promoting generation of $\cdot O_2^-$ with extended lifetime and moderate oxidation ability. Direct evidence supporting this mechanism was provided by operando Ni K-edge X-ray absorption near-edge structure (XANES), which revealed an approximately 0.5 eV edge shift for Ni single atoms under irradiation, while NiO_x nanoparticles showed no detectable change, indicating that photogenerated electrons are preferentially transferred to the isolated Ni sites. Temperature-programmed desorption of oxygen (O_2-TPD) further showed that O_2 adsorption predominantly occurs on Ni single atoms rather than oxygen vacancies. Under air and 365 nm irradiation, the system enables highly selective C–C bond cleavage of glycerol to glycolaldehyde with selectivity approaching the theoretical limit (Fig. 27a). A weak adsorption-rapid desorption mechanism further suppresses over-oxidation of the C_2 product, demonstrating the potential of precisely engineered single-atom sites to regulate ROS and enable highly selective photocatalytic C–C bond cleavage in biomass conversion.

Another representative example is the C–H chlorination reaction reported in 2025 by Liu, Su, and co-workers.[90] In this work, Pt_1-TiO_2 nanorod array photoanodes are constructed by anchoring single-atom Pt on TiO_2 nanorods with oxygen vacancies and Ti^{3+}. The 1D architecture decouples light absorption from hole transport, enabling selective C–H chlorination using NaCl under a mild applied bias. Employing cyclohexane as a model substrate, the system achieves a production rate of 104.2 μmol·cm^{-2}·h^{-1}, monochlorination selectivity of 87.5%, Faradaic efficiency of 58.8%, and an AQE of 43%. The protocol exhibits a broad substrate scope, tolerating cycloalkanes, electron-rich arenes, and heteroaromatic substrates such as pyridines, consistently delivering high conversions and selectivity (Fig. 27b). Mechanistic investigations further revealed that Cl^- preferentially adsorbs on Pt single atoms to form Pt–Cl bonds, as evidenced by *in situ* Raman and XAS, DFT calculations further supported this preferential interaction, showing negative Cl formation energies on Pt (−0.66 to −1.06 eV), in contrast to the positive values obtained on TiO_2. Radical trapping experiments and EPR spectroscopy identified ·Cl as the key active species, and a kinetic isotope effect of 1.32 supported C–H hydrogen abstraction as the rate-determining step. Nevertheless, the surface coverage and lifetime of ·Cl species at the Pt sites remain to be quantitatively established.

Recently, Beller, Das and co-workers reported a notable Fe-based heterogeneous photocatalytic system for alkene oxidative cleavage using CO_2 as the sole oxygen donor, which is distinctive as CO_2 is normally used as a C1 feedstock.[91] The catalyst, Fe@f-gC_3N_4, features a mixture of atomically dispersed Fe species and Fe oxide nanoparticles, and is prepared using 2-amino-5-(trifluoromethyl)benzonitrile to produce a fluorine-modified CN support with an electron-deficient environment

Green Chemistry Accepted Manuscript

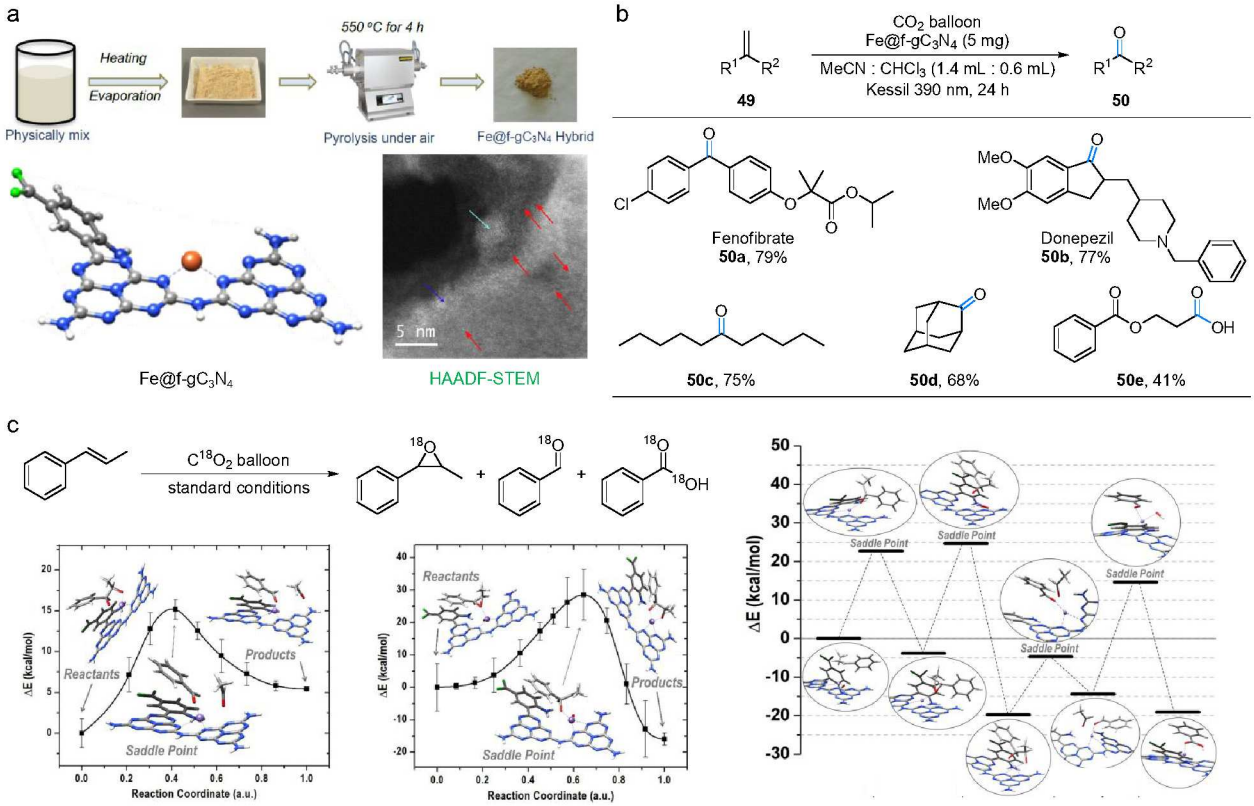

Fig. 28 (a) Preparation and characterization of Fe@f-gC_3N_4 (red arrows indicating single iron atoms, a blue arrow indicating surface enriched Fe species and cyan arrow indicating Fe containing nanoparticle). (b) Selected examples for cleavage of alkenes using CO_2. (c) Mechanistic studies with $C^{18}O_2$-labeling and DFT calculations. Reproduced with permission.[91] Copyright 2026, American Association for the Advancement of Science.

(Fig. 28a). In this system, the electron-deficient Fe environment promotes interaction with the oxygen atom of CO_2, generating Fe-bound oxygen species that transfer oxygen to alkenes. Under optimized conditions, various alkenes with different functional groups can be converted to the corresponding ketones or carboxylic acids, such as the synthesis of Fenofibrate (**50a**), donepezil (**50b**) etc. (Fig. 28b). Mechanistic studies including DFT calculations suggested a stepwise oxygen-transfer and C–C cleavage pathway. Kinetic experiments detected epoxide and benzaldehyde intermediates before benzoic acid accumulation, while $C^{18}O_2$-labeling confirmed that the oxygen atoms in the intermediates and final product originated from CO_2. Quantum mechanical (QM) calculations further indicated that CO_2 is chemisorbed and activated on Fe@f-gC_3N_4 to generate catalyst-bound oxygen species, which react with C=C-coordinated alkenes to form epoxide intermediates. Subsequent ring opening gives a dioxygen intermediate, followed by C–C bond cleavage to aldehydes and final oxidation to carboxylic acids by an additional oxygen atom derived from another activated CO_2 molecule (Fig. 28c). However, it should be noted that the catalyst comprises a mixture of atomically dispersed Fe species and Fe oxide nanoparticles, with extended X-ray absorption fine structure (EXAFS) analysis further revealing Fe aggregation after the reaction. This structural complexity and dynamic evolution raise the question of whether the computational model fully captures the active species under working conditions.

6. Characterization, stability, controversies and metrics

6.1 Characterization: current practices and limitations

Structural characterization of SAC-based photocatalysts through out this review has relied primarily on a combination of electron microscopy and X-ray spectroscopy. Aberration-corrected HAADF-STEM is the most frequently employed technique for directly visualizing atomically dispersed metal species as bright spots against the support,[92] and has been applied to many of the system discussed in this review. XPS complements these observations by providing information on the chemical state of the metal centers and their interaction to the support, most commonly through shifts in the metal 2p or 3d binding energies. XAS, including XANES and EXAFS, offers detailed information on the local coordination environment and oxidation state of single atoms, and has been indispensable in cases where the distinction between single atoms and small clusters is critical.[93] The use of XAS, however, is notably inconsistent across the literature: while some studies provide

Green Chemistry Accepted Manuscript

full quantitative fitting of coordination numbers and bond distances, others rely solely on HAADF-STEM and XPS to claim single-atom dispersion, without complementary X-ray absorption analysis. This inconsistency complicates cross-system comparisons and, in some cases, leaves the single-atom nature of the catalyst insufficiently established.

Beyond structural verification, understanding the photophysical properties of SACs is essential for establishing structure-performance relationships. UV-vis diffuse reflectance spectroscopy (UV-vis DRS), often combined with Mott-Schottky measurements, is routinely used to determine the light-absorption range and band-edge positions of the semiconductor support, and to assess how metal incorporation alters the electronic band structure. Steady-state PL and time-resolved PL (TRPL) spectroscopy provide insights into charge-carrier recombination dynamics, with decreased PL intensity and shortened lifetimes often associated with altered charge-transfer and recombination dynamics following metal incorporation. Electrochemical impedance spectroscopy (EIS) and transient photocurrent measurements further evaluate charge-transfer resistance and photoinduced charge-separation behaviour, and have been widely employed to compare the performance of single-atom catalysts against their nanoparticle counterparts.[94] EPR spectroscopy, often used in conjunction with spin-trapping or quenching agents such as DMPO and TEMPO, plays a central role in identifying reactive oxygen species including $\cdot O_2^-$, $^1O_2$, and ·OH, and in monitoring the dynamic redox states of metal centers under irradiation.[95] Collectively, these photophysical techniques serve as a critical bridge linking the structural features of SACs to their photocatalytic performance.

Despite the widespread application of these techniques, the characterization of SAC-based photocatalysts would benefit from greater consistency across the field. The most immediate issue is the uneven application of XAS, making it difficult to compare coordination environments across different systems. Photophysical characterization is similarly variable, some works report only steady-state PL, while others provide comprehensive TRPL, EIS, and transient photocurrent data, and only a minority employ *in situ* or operando techniques to track the dynamic evolution of single-atom sites under actual reaction conditions.[96] This lack of methodological consistency hinders the establishment of reliable structure-activity relationships and can complicates both the rigorous identification of single-atom sites and meaningful comparisons of their photocatalytic behaviour across different systems. A more unified characterization framework, combining complementary structural, photophysical, and operando techniques, would therefore be beneficial in advancing the field toward more rational catalyst design.

6.2 Catalyst stability and structural evolution

Catalyst stability is central to the green-chemistry value of single-atom photocatalysis. The advantages commonly associated with SACs, including catalyst recovery, reduced metal consumption, minimized metal contamination, and improved reusability, are only meaningful when the isolated metal sites and the semiconductor support remain sufficiently stable under reaction conditions. However, photocatalytic organic transformations often involve prolonged irradiation, redox-active substrates, oxygen, water, acids or bases, sacrificial reagents and ligands. These factors can induce metal leaching, aggregation, changes in oxidation state, coordination restructuring or support degradation.[97,98] Therefore, the stability of SAC-based photocatalysts should not be inferred solely from their heterogeneous nature.

A useful distinction should be made between catalytic stability and structural stability. Catalytic stability refers to the retention of activity and selectivity over repeated cycles, whereas structural stability requires direct evidence that the isolated metal atoms, their coordination environment and the support structure are preserved during or after photocatalysis. These two aspects are related but not equivalent. Several systems discussed in this review exhibit retained catalytic performance over multiple cycles, but the level of post-reaction structural verification varies considerably, which indicates that activity retention alone does not necessarily prove the preservation of isolated single-atom sites. In contrast, some studies provide more quantitative stability information; for instance, Ni/TiO_2-catalyzed enamide sulfonation maintained 84% yield after five cycles with minimal Ni leaching of 0.1-0.5 ppm. Such data are valuable, but they also highlight the need for more consistent reporting of metal leaching, aggregation and post-reaction structural evolution across different SAC systems.

Several possible deactivation or restructuring pathways should be considered in SAC-based photocatalysis.[97-99] First, isolated metal atoms may migrate and aggregate into clusters or nanoparticles under irradiation, especially in reductive environments or when the metal-support interaction is insufficiently strong. Second, metal leaching may occur in polar solvents or in the presence of strongly coordinating substrates, amines, phosphineoxides, carboxylates, halides, or Lewis-acid additives. Third, the coordination environment of single atoms may undergo dynamic restruction during catalysis, potentially generating catalytically relevant species that differ from the initially characterized structure. Fourth, the semiconductor support itself may undergo photocorrosion, oxidation, defect evolution, or surface fouling during long-term irradiation. This issue is particularly relevant for sulfide- and CN-based photocatalysts, where changes in surface defects or local coordination environments can strongly influence charge separation and radical generation.

Future studies should therefore evaluate SAC stability using a combination of catalytic and structural criteria. Recycling experiments should be accompanied by metal leaching analysis of the reaction solution, post-reaction HAADF-STEM to assess aggregation, XPS and XAS to monitor changes in oxidation state and coordination environment, and, where appropriate, hot-filtration or filtrate-activity tests to evaluate the possible contribution of leached homogeneous species. Long-term irradiation experiments under realistic reaction conditions are also important because short recycling tests may not reveal slow photocorrosion or gradual site restructuring. Operando

Green Chemistry Accepted Manuscript

XAS, *in situ* EPR, and time-resolved photophysical measurements would further help determine whether the initially characterized single-atom sites remain structurally intact and electronically stable during catalytic turnover. Establishing such stability criteria is essential not only for validating mechanistic assignments but also for enabling meaningful comparisons of catalytic performance, durability and sustainability across different single-atom photocatalytic systems.

6.3 Unresolved controversies and limitations

Despite rapid progress, several unresolved controversies and limitations remain in SAC-mediated photocatalytic organic synthesis. A central issue is the assignment of the true origin of catalytic activity. In most photocatalytic systems, catalytic performance arises from the combined effects of light absorption, charge separation at metal-support interfaces, substrate adsorption, radical generation, and interfacial electron transfer. Therefore, isolated metal atoms should not always be viewed simply as direct catalytic centers. In many cases, they are better described as components of interfacial catalytic ensembles that regulate the electronic structure and charge-transfer behaviour of the support. This more nuanced view is exemplified by systems in which single-atom sites primarily function as electronic modulators rather than direct substrate-conversion centers, such as the oxidative coupling of benzylamines with embedded Cu1@HCNS rather than the surface-loaded Cu1/HCNS.

The relationship between metal nuclearity and catalytic performance also requires careful interpretation. Clusters, nanoparticles, adjacent single atoms, or mixed single-atom/nanoparticle interfaces may be advantageous when reactions require multi-electron transfer, cooperative adsorption or sequential activation of multiple substrates. Thus, the key question is not whether single atoms are universally superior, how the nuclearity and spatial arrangement of metal sites can be matched to the elementary steps of a given photochemical transformation. This perspective is increasingly reflected in recent studies employing neighbouring single atoms, diatomic sites, or cooperative single-atom/nanoparticle architectures to regulate complex reaction pathways.

Methodological rigor is another area that requires further strengthening. Because photocatalytic reactions are highly sensitive to wavelength, photon flux, irradiation geometry, temperature, mass transfer, catalyst dispersion, and reactor configuration, apparent activity differences may arise from experimental conditions rather than intrinsic catalytic properties. More complete control experiments are therefore needed to disentangle single-atom effects from support effects, defect effects, morphology effects, homogeneous metal contributions, and possible cluster or nanoparticle contributions. For organic synthesis, the evaluation of method generality should also consider substrate diversity, functional-group tolerance, reaction concentration, scale, catalyst loading, and the use of additives, sacrificial reagents, or specific solvents. Transparent reporting of these factors will enable more reliable mechanistic conclusions and cross-system comparisons.

Mechanistic pathways in SAC photocatalysis often require multi-evidence validation. Radical and ROS-mediated transformations may involve holes, superoxide, $^1O_2$, ·OH, surface-bound oxygen species, substrate-derived radicals, or radical cation intermediates, and these species may coexist under irradiation. Scavenger experiments and EPR spin trapping provide valuable initial information, but they are not always sufficient to establish the dominant productive pathway. Similarly, additives can influence not only substrate activation, but also charge recombination, radical stability, surface adsorption, or local proton/electron balance. A stronger mechanistic assignment therefore benefits from the integration of kinetic analysis, isotope labeling, wavelength-dependent activity tests, operando spectroscopy, time-resolved photophysical measurements, and theoretical modelling.

Overall, these issues should be viewed not as weaknesses of individual studies, but as natural challenges for a rapidly developing field at the interface of single-atom catalysis, semiconductor photocatalysis, and organic synthesis. Addressing them will help move SAC-mediated photocatalytic organic synthesis from empirical catalyst screening toward more predictive and rational catalyst and reaction design. Such mechanistic rigor is also essential for establishing meaningful performance benchmarks and sustainability metrics, as discussed in the following section.

6.4 Performance evaluation and sustainability metrics

Quantitative benchmarking is essential for assessing SAC-mediated photocatalytic organic synthesis, but such comparisons require careful interpretation. In organic transformations, yield, conversion, selectivity, and substrate scope remain fundamental indicators of synthetic utility. However, these parameters alone are insufficient for benchmarking the intrinsic performance of SAC-based photocatalysts. The studies discussed in the preceding sections show that reported systems often differ substantially in reaction type, substrate structure, catalyst composition, support material, metal loading, light source, wavelength, photon flux, solvent, atmosphere, reactor configuration, reaction scale, and product analysis. Therefore, direct ranking of distinct catalytic systems, solely by TOF, TON, selectivity, or quantum efficiencies may be scientifically misleading.[100,101] Moreover, most studies report only a subset of the relevant metrics. These metrics are most meaningful when used to compare closely related catalysts within the same reaction system under identical or carefully controlled conditions. For broader cross-system comparison, they should be interpreted as contextual performance descriptors rather than absolute measures of catalyst superiority.

From a green-chemistry perspective, the environmental advantages of SAC-based photocatalysis should also be evaluated using quantitative metrics wherever possible. SACs offer several potential benefits, including high theoretical atom utilization, reduced precious-metal consumption, mild light-

Green Chemistry Accepted Manuscript

 This journal is © The Royal Society of Chemistry 20xx

driven reaction conditions, catalyst recovery, and decreased reliance on stoichiometric oxidants or reductants. Nevertheless, these advantages should not be regarded as intrinsic to all SAC-based photocatalytic systems. Quantitative or semi-quantitative indicators such as E-factor, PMI, life-cycle assessment (LCA), energy input, solvent consumption, sacrificial reagent demand, catalyst lifetime, metal leaching, and catalyst recovery efficiency are needed to assess whether a given protocol is genuinely greener than conventional alternatives.[11,102] At present, however, comprehensive E-factor, PMI, or LCA values are rarely reported in primary studies on photocatalytic organic synthesis. Their retrospective calculation for all reported SAC systems would require assumptions regarding work-up and purification, solvent recovery, catalyst synthesis, light-energy consumption, photon flux, waste streams, catalyst lifetime, and full mass balance. Such assumptions are highly dependent on the chosen system boundary and may lead to misleading comparisons if applied inconsistently across different reports. Thus, the scarcity of these metrics should be regarded as a field-wide reporting gap rather than a limitation that can be fully resolved by retrospective estimation in a review article.

A more practical way forward is to establish a unified reporting framework for SAC-mediated photocatalytic organic synthesis. Future studies should report catalytic metrics such as conversion, isolated yield, chemo-, regio- or stereoselectivity, TON, TOF, reaction rate normalized to catalyst mass and metal content, substrate-to-catalyst ratio, reaction concentration, and scale. Photochemical parameters, including light source, wavelength, light intensity or photon flux, AQY or QE, irradiation geometry, reactor configuration, and temperature control, should also be provided whenever possible. In parallel, durability and sustainability descriptors should include oxidant or reductant requirements, sacrificial reagents, solvent use, catalyst recovery efficiency, recyclability, metal leaching, post-reaction structural characterization, catalyst lifetime, and E-factor or PMI when sufficient data are available. Such a framework would allow SAC photocatalysis to be evaluated not only by activity and selectivity, but also by photon efficiency, durability, practicality, and genuine green-chemistry benefit.

7. Conclusions and perspectives

Although still in its infancy, single-atom photocatalysis has already demonstrated considerable power and great potential for sustainable organic synthesis (Table 1). Compared with conventional nanoparticle-based or bulk heterogeneous photocatalysis, it enables heterogeneous photocatalytic processes to be controlled with much higher precision. Beyond expanding the scope of accessible reaction types, these studies collectively reveal emerging structure-reactivity relationships, in which the coordination environment and interfacial electronic structure of isolated metal centers govern key elementary steps, including charge transfer, radical generation, and intermediate stabilization. Notably, distinct reaction pathways can be selectively accessed through the precise modulation of single-atom sites and support interactions under light irradiation, highlighting the unique ability of SAC photocatalytic systems to combine molecular-level control with the robustness of heterogeneous catalysis. These insights not only unify mechanistic understanding across different reaction classes but also provide a conceptual foundation for the rational design of next-generation heterogeneous photocatalysts for selective organic synthesis. Importantly, beyond these mechanistic advances, SAC photocatalysis also offers significant sustainability advantages, including high atom utilization, mild reaction conditions, catalyst recyclability, and the potential to reduce reliance on stoichiometric oxidants or reductants. Considering the diversity of single metal atoms, the continued expansion of available semiconductor supports (particularly beyond the CN, CdS, and TiO_2 systems discussed in this review), the wide range of material-fabrication techniques, the synergistic interactions between single atoms and support materials, and the rapid emergence of metallaphotoredox catalysis,[103] single atom photocatalysis is poised for a bright future.

Nevertheless, several key challenges remain that need be addressed to further expand the scope and practical application of this emerging field, and to establish SACs as cornerstone materials for sustainable photocatalytic organic synthesis:

(1) The metal loading of most SAC systems remains relatively low, which can limit catalytic activity. The development of high-loading SACs while maintaining atomic dispersion is therefore an important research direction. Achieving this goal requires improved strategies for stabilizing isolated atoms at higher densities without aggregation. Approaches such as defect engineering, heteroatom-rich supports, and spatial confinement within an alternative design philosophy is to dilute the catalytic sites over very high-surface-area supports such as mesoporous materials, MOFs and COFs, so that adjacent metal atoms are spatially separated, thereby reducing the likelihood of aggregation even at elevated loadings.

(2) Many photocatalytic organic transformations involve multiple elementary steps that may benefit from cooperative catalysis. The design of cooperative multi-atom catalytic systems therefore represents another promising direction. Dual-atom catalysts or spatially adjacent active sites can provide complementary functionalities, enable efficient activation of substrates and facilitate multi-electron transfer processes. Rational control over coordination environments and atomic-scale spatial arrangements may open new catalytic pathways that cannot be achieved with isolated single-atom sites alone.

(3) Further progress will strongly depend on the development of novel photocatalytic methodologies. Although SACs have demonstrated remarkable activity in several reaction types, the diversity of accessible organic transformations remains limited compared with homogeneous photoredox catalysis. Expanding the scope of SAC-driven reactions, such as C–H functionalization, cascade radical reactions, and late-stage functionalization of complex molecules, will greatly enhance their synthetic utility.

(4) As sustainability becomes an increasingly important criterion for catalytic technologies, demonstrating the environmental advantages of single atom photocatalysis requires more than high catalytic performance. Long-term catalyst stability, metal leaching, catalyst recyclability, and standardized green chemistry metrics, including E-factor, PMI, and LCA, should be systematically evaluated.

(5) Scale-up and practical production should receive greater attention in future single-atom photocatalytic organic synthesis.

Green Chemistry Accepted Manuscript

Table 1 Single-atom photocatalytic organic transformations

Reaction	Catalyst	Support	Light source	[Oxi]/[red] or sacrificial reagent	Solvent	Maximum Scale	Ref
Benzylamine oxidative coupling reactions	Cu1@HCNS	HCNSs	visible light	H_2O	acetonitrile	2 mmol	24
	CoSAS@CD	carbon quantum dots	visible light	O_2	acetonitrile	1 mmol	25
	CoP@POC	porphyrin-based porous organic cage	visible light	O_2	acetonitrile	1 mmol	26
	PdSA-ZIS	$ZnIn_2S_4$ nanosheets	visible light	H_2O	acetonitrile	-	27
	Ce-SA-C_3N_4	CN	420-780 nm	O_2	acetonitrile	0.27 mmol	28
	Ni/Ce-CN	doped CN	Xe lamp (> 320 nm)	O_2	acetonitrile	0.1 mmol	29
Alcohols and amines coupling	Ni-SA@PCN	CN	420 nm	O_2	trifluorotoluene	0.5 mmol	30
Acetone to 2,5-hexanedione	Pt-TiO_2	TiO_2	Xe lamp	none	20 vol% acetone aqueous solution	-	31
	Pt-TiO_2	TiO_2	365 nm	H_2O	acetone aqueous solution	7 mL acetone	32
Methanol coupling to ethylene glycol	RhSA-WZ/$Zn_{0.67}Cd_{0.33}S$	ZnCdS nanorod	Xe lamp (320-780 nm)	none	methanol aqueous solution	4.0 mL CH_3OH	33
Methane coupling to ethane	Pt SA nest on TiO_2	TiO_2	Xe lamp	none	none	-	34
Sulfonation of alkenes	CNH	CN	460 nm	air	acetonitrile	0.5 mmol	35
Decarboxylative Heck-type coupling	Co_{SA}-K-PHI	potassium poly(heptazine imide) (K-PHI)	460 ± 5 nm	none	toluene	0.2 mmol	36
(Hetero)arenes coupling with nucleophiles	Pt-g-C_3N_4	CN	370 nm	none	acetonitrile	50 mmol	37
Amination coupling of aryl halides with sodium azide	Ni-mpg-CN_x	CN	447 ± 20 nm	Et_3N	methanol aqueous solution	0.4 mmol	41
Homocoupling of benzyl bromide	SA-Cu/TiO_2(B)–V_O	TiO_2	Xe lamp	isopropanol/ethanol/methanol	isopropanol/ethanol/methanol with 10 vol% water	0.15 mmol	42
N-formylation of amines	Pt-Bi/CeO_{2-x}	CeO_2	Xe lamp	CO_2, $PhSiH_3$	*N*,*N*-dimethylformamide	0.47 mmol	43
Cyclization of levulinic acid to γ-valerolactone	Pt/GFs	graphitic frameworks	UV lamp	Water, EtOH, formic acid, MeOH, 2-PrOH	aqueous solution	-	44
Reductive coupling of aryl iodides to ketones	Pd_{SA}-PCN	CN	370 nm	H_2O	acetonitrile	decagram-scale	45

Green Chemistry Accepted Manuscript

Reaction	Catalyst	Support	Light source	[Oxi]/[red] or sacrificial reagent	Solvent	Maximum Scale	Ref
Dehalogenation–arylation and hydro-dehalogenation of organic halides	SAAg	AgF/AgI surface	425 nm	none	benzene, acetonitrile	20 mg	46
Borylation of aryl iodides	$Ag_{EG}/Mg(OH)_2$	$Mg(OH)_2$	425 ± 7 nm	none	acetonitrile	1.0 g, 4.3 mmol	47
	$Ag(0)/SiO_2$	SiO_2	425 nm	none	acetonitrile	1.0 g, 4.3 mmol	48
Cross-coupling of aryl halides with alcohols	C_3N_4–Ni	CN	> 400 nm	none	*N,N*-dimethylacetamide	1.99 g, 10 mmol	49
	Ni-mpg-CN_x	CN	447 ± 20 nm	none	ethanol	0.2 mmol	50
	Ni_1-mpg-CN_x	CN	427 nm	none	*N,N*-dimethylacetamide	0.4 mmol	51
Cross-coupling of aryl bromides with amines	NiSAC/CN	CN	blue light	none	*N,N*-dimethylacetamide	0.1 mmol	52
C–O coupling of carboxylic acids and alkyl halides	Ni_{SA}-nCN_x	CN	white light	none	acetone	0.45 mmol	53
Suzuki coupling and Ni-catalyzed C–O bond formation	M_1/C_3N_4 (M = Pd, Ni)	CN	blue light	none	*N,N*-dimethylacetamide, acetonitrile	0.08 mmol/0.1 mmol	54
N-alkylation of amines	CdS-Pd SAs	CdS	Xe lamp (> 420 nm)	none	acetonitrile	0.16 mmol	55
	Bi–S_3/S-V_s	$ZnIn_2S_4$ (S-V_s)	455 nm	none	benzyl alcohol	0.55 mmol	56
Amination of α-hydroxy acids	Ru_1/CdS	CdS	(420–780 nm)	none	ammonia solution	20 mmol	57
Heck coupling	Pd_1/g-C_3N_4, Ni_1/g-C_3N_4	CN	Xe lamp	none	*N,N*-dimethylformamide	0.1 mmol	58
Hydrogenation of styrene to ethylbenzene	Pd_1-mpg-C_3N_4	CN	427 nm	H_2O	1,4-dioxane and water	0.3 g (2.9 mmol)	62
Hydrogenation of C=C bonds	Pd-mpg-CN	CN	427 nm	H_2O	1,4-dioxane and water	0.2 g (0.96 mmol)	63
	Pd_2-mpg-C_3N_4	CN	427 nm	H_2O	1,4-dioxane and water	0.15 mmol	64
Semihydrogenation of alkynes	Ni–N/CN	CN	420 nm	H_2O	acetonitrile and D_2O	0.65 mmol	65
Reduction of 4-chlorophenol to cyclohexanone	Pd/TiO_2	TiO_2	365 nm	MeOH/H_2O	MeOH-H_2O	2.18 µmol	66
Site-selective sulfonation of enamides	Ni/TiO_2	TiO_2	460 nm	O_2	acetonitrile	5 mmol (gram-scale)	67
Hydrophosphinylation of alkenes and alkynes	Cu(I)–N_4	CN	390 nm	none	*N,N*-dimethylformamide	1 mmol	68

Green Chemistry Accepted Manuscript

Reaction	Catalyst	Support	Light source	[Oxi]/[red] or sacrificial reagent	Solvent	Maximum Scale	Ref
Cycloaddition of CO_2 and epoxides to cyclic carbonates	Al–N–C	porous carbon nanosheets	full-spectrum	none	*N,N*-dimethylformamide	0.67 mmol	69
Benzene oxidation	SA-Cu-TCN	CN	> 420 nm	H_2O_2	acetonitrile	4.5 mmol	73
Benzyl alcohol oxidation	CoPc/P-CN	CN	Xe lamp	O_2	acetonitrile	0.2 mmol	74
HMF oxidation	Cu SAs/p-CNS	CN	455 nm ± 10 nm	O_2	acetonitrile	0.05 mmol	75
Ethanol to 1,1-diethoxyethane (DEE)	PdPSA-CdS	CdS nanorods	Xe lamp	none	ethanol	100 mL ethanol	76
Benzyl alcohol oxidation	Pt_1/TiO_2-MP	TiO_2	Xe lamp	O_2	acetonitrile	1 mmol	77
Methanol dehydrogenation	Pd_1 + Pd cluster/CdS	CdS	455 nm	none	methanol	50 mL methanol	78
Benzyl alcohol oxidation	$Ag_1@CN_x$	CN	450 nm	none	acetonitrile	0.18 mmol	79
Benzaldehyde oxidation	SA-Pt	CN	Xe lamp	H_2O	deionized water	39.4 mmol	80
Glucose oxidation	$Fe–N_x$	CN	Xe lamp	peroxymonosulfate	water	0.015 mmol	81
Ethylbenzene oxidation	$Fe–N_4$	CN	Xe lamp (> 420 nm)	O_2	acetonitrile	0.5 mmol	82
Methane oxidation	$Co–C_2N_2$	CN	Xe lamp (300–780 nm)	H_2O	water	gram-scale	83
Benzylic C(sp^3)–H oxidation	Y_1/TiO_2	TiO_2	Xe lamp (full-spectrum)	O_2	acetonitrile	10 mmol	84
Toluene oxidation	$Pd–O_3/Bi_2WO_6$	Bi_2WO_6	405 nm	O_2	acetonitrile	1 mmol	85
Cyclohexanone oxidation	Ir_1/Ti-α-Fe_2O_3	Ti-doped α-Fe_2O_3	Xe lamp	H_2O	aqueous KOH solution	-	86
Propane dehydrogenation	CuPt plasmonic single-atom alloys	SiO_2	585 ± 50 nm	none	none	total flow rate of 50 sccm	87
	Cu_1/TiO_2	TiO_2	Xe lamp	none	none	total flow rate of 12 mL/min	88
C–C bond cleavage	Ni/TiO_2	TiO_2	365 nm	O_2	water	0.75 mmol	89
C–H chlorination reaction	Pt_1-TiO_2	TiO_2	365 nm	NaCl	acetonitrile and water	0.2 mmol	90
Oxidative cleavage of alkenes	Fe@f-gC_3N_4	CN	456 nm	CO_2	acetonitrile and chloroform	0.2 mmol	91

This table summarizes the photocatalytic organic transformations driven by SACs. sccm (standard cubic centimeters per minute). "-" means that data are not available.

Most current SAC-based reactions are still conducted in small-scale batch reactors, where limited light penetration, inefficient mixing and solid handling restrict practical application. Flow technologies, particularly high-speed circulation flow systems,[38] offer a promising solution by maintaining heterogeneous photocatalysts in suspension, reducing clogging and enabling extended irradiation without being

Green Chemistry Accepted Manuscript

This journal is © The Royal Society of Chemistry 20xx

limited by reactor volume. Recent advances in colloidal nanofluid materials also provide new opportunities for handling semiconductors under flow conditions without clogging.[104] Other reactor designs are also explored for integrating heterogeneous photocatalysis with scalable synthesis, including packed-bed reactors, 3D-printed structured catalysts, and falling-film reactors. These technologies respectively enhance light transmission, circumvent washcoating adhesion issues, and provide validated scale-up models, thereby broadening scale-up options beyond flow chemistry.[105-107] Future efforts should integrate catalyst design with reactor engineering, focusing on photostability, metal leaching control, photon efficiency, catalyst recovery and automated semicontinuous production.

(6) Finally, despite rapid advances in characterization techniques and computational approaches, the mechanistic understanding of SAC-based photocatalysis remains elusive. Key questions such as the dynamic evolution of single-atom sites under operating conditions, the nature of metal-support charge transfer, and the selectivity control of ROS are still not fully resolved. A deeper mechanistic understanding, particularly through operando and time-resolved techniques combined with theoretical modeling, will be essential for the rational design of next-generation single-atom photocatalysts with improved activity and selectivity.

Author contributions

Yang Shi: content categorization, review writing, figure editing, conceptualization. Wei Fang: review writing, figure editing. Gan Wang: review writing, figure editing. Guangmei Gan: review writing. Jie Wu: project administration, conceptualization, review writing, supervision, funding acquisition.

Conflicts of interest

There are no conflicts to declare.

Abbreviations

AQE	Apparent quantum efficiency
AQY	Apparent quantum yield
CDCs	Cross-dehydrogenative couplings
CN	Carbon nitrides
g-C_3N_4	Graphitic carbon nitride
COF	Covalent organic framework
DEE	1,1-Diethoxyethane
DFF	2,5-Diformylfuran
DFT	Density functional theory
EG	Ethylene glycol
EIS	Electrochemical impedance spectroscopy
EnT	Energy transfer
EPR	Electron paramagnetic resonance
ESR	Electron spin resonance
EXAFS	Extended X-ray absorption fine structure
GVL	γ-Valerolactone
HAADF-STEM	High-angle annular dark-field scanning transmission electron microscopy
HDN	2,5-Hexanedione
HMF	5-Hydroxymethylfurfural
HSCF	High-speed circulation flow
ICP-MS	Inductively coupled plasma mass spectrometry
ICP-OES	Inductively coupled plasma optical emission spectroscopy
LA	Levulinic acid
LCA	Life-cycle assessment
LMCT	Ligand-to-metal charge transfer
LSPR	Localized surface plasmon resonance
MLCT	Metal-to-ligand charge transfer
MOF	Metal-organic framework
MS	Molten-salt
O_2-TPD	Temperature-programmed desorption of oxygen
PCN	Polymeric carbon nitride
PDH	Propane dehydrogenation
PEC	Photoelectrocatalytic
PILE	Photoinduced ligand exchange
PL	Photoluminescence
PMI	Process mass intensity
QM	Quantum mechanical
RHE	Reversible hydrogen electrode
ROS	Reactive oxygen species
SACs	Single-atom catalysts
SET	Single-electron transfer
SMSI	Strong metal-support interactions
TEOA	Triethanolamine
TFO	Ti-doped α-Fe_2O_3
TOF	Turnover frequency
TON	Turnover number
TRPL	Time-resolved PL
UPS	Ultraviolet photoelectron spectroscopy
UV-vis DRS	UV-vis diffuse reflectance spectroscopy
WZ/ZB	Wurtzite and cubic zinc-blende
XANES	X-ray absorption near-edge structure
XAS	X-ray absorption spectroscopy
XPS	X-ray photoelectron spectroscopy

Data availability

This review does not report new experimental or computational data. All information discussed in this article is derived from previously published studies.

Acknowledgements

We acknowledge financial support from the Prime Minister's Office of Singapore under its NRF-CRP Programme (NRF-CRP29-2022-0004), the Agency for Science, Technology and Research (A*STAR) under its MTC IRG Grant (Project M22K2c0082), the National Natural Science Foundation of China (22371200) and the NUS (Suzhou) Research Institute. We also acknowledge financial support from Pfizer (A-8002093-00-00).

References

Green Chemistry Accepted Manuscript

1 B. Qiao, A. Wang, X. Yang, L. F. Allard, Z. Jiang, Y. Cui, J. Liu, J. Li and T. Zhang, *Nat. Chem*., 2011, **3**, 634–641.
2 X.-F. Yang, A. Wang, B. Qiao, J. Li, J. Liu and T. Zhang, *Acc. Chem. Res*., 2013, **46**, 1740–1748.
3 L. Liu and A. Corma, *Chem. Rev*., 2018, **118**, 4981–5079.
4 Y. Shi, Y. Zhou, Y. Lou, Z. Chen, H. Xiong and Y. Zhu, *Adv. Sci*., 2022, **9**, 2201520.
5 J. Liu, *ACS Catal*., 2017, **7**, 34–59.
6 C.-F. Li, W.-G. Pan, Z.-R. Zhang, T. Wu and R.-T. Guo, *Small*, 2023, **19**, 2300460.
7 Z.-H. Xue, D. Luan, H. Zhang and X. W. (David) Lou, *Joule*, 2022, **6**, 92–133.
8 Q. Wang, D. Zhang, Y. Chen, W.-F. Fu and X.-J. Lv, *ACS Sustainable Chem. Eng*., 2019, **7**, 6430–6443.
9 L. Marzo, S. K. Pagire, O. Reiser and B. König, *Angew. Chem. Int. Ed.*, 2018, **57**, 10034–10072.
10 J. C. Colmenares and R. Luque, *Chem. Soc. Rev*., 2014, **43**, 765–778.
11 R. A. Sheldon, *Green Chem*., 2017, **19**, 18–43.
12 Y. Zhang, J. Zhao, H. Wang, B. Xiao, W. Zhang, X. Z hao, T. Lv, M. Thangamuthu, J. Zhang, Y. Guo, J. Ma, L. Lin, J. Tang, R. Huang and Q. Liu, *Nat. Commun*., 2022, **13**, 58.
13 S.-M. Wu and P. Schmuki, *Adv. Mater*., 2025, **37**, 2414889.
14 W. Hu, H. Yang and C. Wang, *RSC Adv*., 2023, **13**, 20889–20908.
15 L. Ran, Z. Li, B. Ran, J. Cao, Y. Zhao, T. Shao, Y. Song, M. K. H. Leung, L. Su and J. Hou, *J. Am. Chem. Soc*., 2022, **144**, 17097–17109.
16 C. Mu, C. Lv, X. Meng, J. Sun, Z. Tong and K. Huang, *Adv. Mater. Interfaces*, 2023, **10**, 2201842.
17 N. A. Romero and D. A. Nicewicz, *Chem. Rev*., 2016, **116**, 10075–10166.
18 A. Sivo, V. Ruta, V. Granata, O. Savateev, M. A. Bajada and G. Vilé, *ACS Sustainable Chem. Eng*., 2023, **11**, 5284–5292.
19 M.-Y. Qi, M. Conte, M. Anpo, Z.-R. Tang and Y.-J. Xu, *Chem. Rev*., 2021, **121**, 13051–13085.
20 V. B. Saptal, V. Ruta, M. A. Bajada and G. Vilé, *Angew. Chem. Int. Ed*., 2023, **62**, e202219306.
21 G. Giannakakis, S. Mitchell and J. Pérez-Ramírez, *Trends Chem.*, 2022, **4**, 264–276.
22 M. B. Gawande, *ACS Sustainable Chem. Eng*., 2026, **14**, 1–2.
23 Y. Yang, J. Lan and J. You, *Chem. Rev*., 2017, **117**, 8787–8863.
24 G. Wang, T. Zhang, W. Yu, R. Si, Y. Liu and Z. Zhao, *ACS Catal*., 2020, **10**, 5715–5722.
25 Q. Wang, J. Li, X. Tu, H. Liu, M. Shu, R. Si, C. T. J. Ferguson, K. A. I. Zhang and R. Li, *Chem. Mater*., 2020, **32**, 734–743.
26 F. Zhang, J. Ma, Y. Tan, G. Yu, H. Qin, L. Zheng, H. Liu and R. Li, *ACS Catal*., 2022, **12**, 5827–5833.
27 P. Wang, S. Fan, X. Li, J. Wang, Z. Liu, Z. Niu, M. O. Tadé and S. Liu, *Nano Energy*, 2022, **95**, 107045.
28 D. Sun, Y. Chen, X. Yu, Y. Yin and G. Tian, *Chem. Eng. J*., 2023, **462**, 142084.
29 X.-D. Zhou and Y.-H. Tian, *J. Mater. Sci.: Mater. Electron*, 2024, **35**, 675.
30 J. Ma, F. Zhang, Y. Tan, S. Wang, H. Chen, L. Zheng, H. Liu and R. Li, *ACS Appl. Mater. Interfaces*, 2022, **14**, 18383–18392.
31 P. Zhou, Y. Chao, F. Lv, K. Wang, W. Zhang, J. Zhou, H. Chen, L. Wang, Y. Li, Q. Zhang, L. Gu and S. Guo, *ACS Catal*., 2020, **10**, 9109–9114.
32 X. Zhou, S. Ye, S. Zhao, H. Song, H. Gong, S. Fan, M. Liu, M. Wang, W. Zhou, J. Liu, S. Yao and L. Lin, *ACS Catal*., 2023, **13**, 11825–11833.
33 L. Wang, Y. Sun, F. Zhang, J. Hu, W. Hu, S. Xie, Y. Wang, J. Feng, Y. Li, G. Wang, B. Zhang, H. Wang, Q. Zhang and Y. Wang, *Adv. Mater*., 2023, **35**, 2205782.
34 P. Zhang, J. Li, H. Huang, X. Sui, H. Zeng, H. Lu, Y. Wang, Y. Jia, J. A. Steele, Y. Ao, M. B. J. Roeffaers, S. Dai, Z. Zhang, L. Wang, X. Fu and J. Long, *J. Am. Chem. Soc*., 2024, **146**, 24150–24157.
35 J. Wen, X. Yang, Z. Sun, J. Yang, P. Han, Q. Liu, H. Dong, M. Gu, L. Huang and H. Wang, *Green Chem*., 2020, **22**, 230–237.
36 Q. Yang, M. Wu, W. Wang, W. Wang, H. Wang, Y. Tang, M. Rueping and Y. Cai, *Chem. Sci*., 2025, **16**, 19154–19163.
37 Y. Shi, X. Hai, L. Cheng, H. Du, X. Yu, H. T. Ang, Jiale Wu, J. Chen, G. Wang, J. Lu and Jie Wu, *Nat. Catal*., 2025, **8**, 1325–1337.
38 C. Liu, L. Song, Q. Liu, W. Chen, J. Xu, M. Wang, Y. Zhang, T. W. Tan, Z. Lei, L. Cheng, S. A. Khan and J. Wu, *Org. Process Res. Dev.,* 2024, **28**, 1964–1970.
39 H. Sun, Y. Yang, Y. Liu, D. Yang, Y. Liu and Z. Sun, *Nanomaterials*, 2026, **16**, 129.
40 L. E. Ehehalt, O. M. Beleh, I. C. Priest, J. M. Mouat, A. K. Olszewski, B. N. Ahern, A. R. Cruz, B. K. Chi, A. J. Castro, K. Kang, J. Wang and D. J. Weix, *Chem. Rev*., 2024, **124**, 13397–13569.
41 A. Vijeta, C. Casadevall and E. Reisner, *Angew. Chem. Int. Ed.*, **2022**, *61*, e202203176.
42 Q. Chen, P. Zheng, H. Liu, Y. Zhang, S. Li, H. Guo, Y. Fang, X. Hu and R. Duan, *Catal. Sci. Technol*., 2024, **14**, 1568–1578.
43 Y. He, P. Bai, S. Yuan, J. Chen, Y. Zhao and Y. Li, *Mol. Catal*., 2024*,* **559***,* 114086.
44 J. Yuan, W. Gao, H. Chen, Y. Yu, Q. Xue, L. Chang, P. Yang, Y. Zhou and B. Cao, *Renewable Energy*, 2025, **248***,* 123050.
45 H. Du, Q. Yu, Y. Miao, J. Ao, J. Wu, K. Fu, Y. Shi, J. Li, J. Ma and J. Wu, *J. Am. Chem. Soc*., 2025, **147**, 47057–47067.
46 W. Wu, E. Cui, Y. Zhang, C. Zhang, F. Zhu, C.-H. Tung and Y. Wang, *ACS Catal*., 2019, **9**, 6335–6341.
47 E. Cui, H. Li, C. Zhang, D. Qiao, M. B. Gawande, C.-H. Tung and Y. Wang, *Appl. Catal. B-Environ*., 2021, **299**, 120674.
48 E. Cui, D. Qiao, H. Li, L. Guo, C.-H. Tung and Y. Wang, *J. Catal*., 2021, **402**, 255–263.
49 X. Zhao, C. Deng, D. Meng, H. Ji, C. Chen, W. Song and J. Zhao, *ACS Catal.*, 2020, **10**, 15178–15185.
50 A. Vijeta, C. Casadevall, S. Roy and E. Reisner, *Angew. Chem. Int. Ed.*, 2021, **60**, 8494–8499.
51 E. Zhao, L. Chen, Q. Zhu, Z. Chen, Y. Wei, W. Zhang, L. Dong, W. Fang and Z. Chen, *Chin. J. Chem*., 2023, **41**, 3281–3289.
52 M. Kwak, J. Bok, B.-H. Lee, J. Kim, Y. Seo, S. Kim, H. Choi, W. Ko, W. H. Antink, C. W. Lee, G. H. Yim, H. Seung, C. Park, K.-S. Lee, D.-H. Kim, T. Hyeon and D. Yoo, *Chem. Sci.,* 2022, **13**, 8536–8542.
53 M. A. Bajada, G. D. Liberto, S. Tosoni, V. Ruta, L. Mino, N. Allasia, A. Sivo, G. Pacchioni and G. Vilé, *Nat. Synth.*, 2023, **2**, 1092–1103.
54 S. Kim, J. Bok, B.-H. Lee, H. Choi, Y. Seo, J. Kim, J. Kim, W. Ko, K.-S. Lee, S.-P. Cho, T. Hyeon and D. Yoo, *ACS Nano*, 2023, **17**, 21470–21479.
55 F. Niu, W. Tu, X. Lu, H. Chi, H. Zhu, X. Zhu, L. Wang, Y. Xiong, Y. Yao, Y. Zhou and Z. Zou, *ACS Catal.*, 2022*,* **12***,* 4481–4490.
56 G. Wang, Y. Liu, J. Zhang, Q. Chen, K. Fang and J. Mao, *J. Mater. Chem. A*, 2022*,* **10***,* 21349–21355.
57 W. Li, X. Zheng, B.-B. Xu, Y. Yang, Y. Zhang, L. Cai, Z.-J. Wang, Y.-F. Yao, B. Nan, L. Li, X.-L. Wang, X. Feng, M. Antonietti and Z. Chen, *Angew. Chem. Int. Ed.*, 2024*,* **63***,* e202320014.
58 X. Zhou, S. Tong and Z. Zhang, *Catal. Sci. Technol.,* 2025*,* **15***,* 3660–3666.
59 A. Zhang, K. Yang, A. Prewette and W. Diao, *Catal. Sci. Technol*., 2025, **15**, 6318–6352.
60 X. Cui and K. Burgess, *Chem. Rev.,* 2005, **105**, 3272–3296.
61 L. M. Wickham and R. Giri, *Acc. Chem. Res.*, 2021, **54**, 3415–3437.
62 E. Zhao, M. Li, B. Xu, X.-L. Wang, Y. Jing, D. Ma, S. Mitchell, J. Pérez-Ramírez and Z. Chen, *Angew. Chem. Int. Ed.*, 2022*,* **61***,* e202207410.
63 E. Zhao, W. Kong, G. Zoppellaro, Y. Yang, B. Nan, L. Li, W. Zhang, Z. Chen, A. Bakandritsos, Z.-J. Wang, M. Beller, R. Zbořil and Z. Chen, *Adv. Mater.*, 2025*,* **37***,* 2504108.

Green Chemistry Accepted Manuscript

This journal is © The Royal Society of Chemistry 20xx

64 E. Zhao, J. M.-Vidal, Y. Yang, S. Mitchell, Y. Zhu, Z. Hu, J.-M. Chen, S.-C. Haw, T.-S. Chan, Z. Fan, Z.-J. Wang, N. López, J. P.-Ramírez and Z. Chen, *J. Am. Chem. Soc.*, 2025, **147**, 2029–2036.
65 T. Jia, D. Meng, R. Duan, H. Ji, H. Sheng, C. Chen, J. Li, W. Song and J. Zhao, *Angew. Chem. Int. Ed.*, 2023, **62**, e202216511.
66 J. Huang, F. Dao, J. Xie, H. Zhang and J. Jiang, *Sep. Purif. Technol.*, 2025, **363**, *132109*.
67 J. Yang, Z. Sun, K. Yan, H. Dong, H. Dong, J. Cui, X. Gong, S. Han, L. Huang and J. Wen, *Green Chem.*, 2021, **23**, 2756–2762.
68 G. Wang, Y. Liu, X. Zhang, X. Zong, X. Zhang, K. Zheng, D. Qu, L. An, X. Qi and Z. Sun, *J. Am. Chem. Soc.*, 2024, **146**, 8668–8676.
69 Q. Yang, H. Peng, Q. Zhang, X. Qian, X. Chen, X. Tang, S. Dai, J. Zhao, K. Jiang, Q. Yang, J. Sun, L. Zhang, N. Zhang, H. Gao, Z. Lu and L. Chen, *Adv. Mater.*, 2021, **33**, 2103186.
70 A. N. Campbell and S. S. Stahl, *Acc. Chem. Res*., 2012, **45**, 851–863.
71 M. K. Panjwani, S. M. Ahmadzai, J. Li, Z. Luo, G. Eshaq, K. Xiao and H. Zeng, *J. Mater. Chem. A*, 2026, **14**, 12509–12539.
72 L. Liu, Y. Liu, X. Li, Y. Zhao, X. Zhang, F. Meng, H. Wang, Y. Huang, L. Wang and C.-D. Wu, *Coord. Chem. Rev*., 2026, **566**, 218196.
73 X. Xiao, Y. Gao, L. Zhang, J. Zhang, Q. Zhang, Q. Li, H. Bao, J. Zhou, S. Miao, N. Chen, J. Wang, B. Jiang, C. Tian and H. Fu, *Adv. Mater*., 2020, **32**, 2003082.
74 X. Chu, Y. Qu, A. Zada, L. Bai, Z. Li, F. Yang, L. Zhao, G. Zhang, X. Sun, Z.-D. Yang and L. Jing, *Adv. Sci.*, 2020, **7**, 2001543.
75 G. Wang, R. Huang, J. Zhang, J. Mao, D. Wang and Y. Li, *Adv. Mater.*, 2021, **33**, 2105904.
76 P. Zhou, Q. Zhang, Y. Chao, L. Wang, Y. Li, H. Chen, L. Gu and S. Guo, *Chem*, 2021, **7**, 1033–1049.
77 N. Sun, J. Song, Q. Tao, E. Kan and L. Kuai, *Microporous Mesoporous Mater.,* 2022, **337**, 111949.
78 Z. Gao, T. Montini, J. Mu, N. Luo, E. Fonda, P. Fornasiero and F. Wang, *J. Am. Chem. Soc.*, 2024, **146**, 24440–24449.
79 A. Moutsiou, A. Olivati, L. A. Cipriano, A. Sivo, S. M. Collins, Q. M. Ramasse, I. S. Kwon, G. D. Liberto, M. Kanso, R. Wojcieszak, G. Pacchioni, A. Petrozza and G. Vilé, *ACS Catal.*, 2025, **15**, 5601–5613.
80 L. Wang, R. Tang, A. Kheradmand, Y. Jiang, H. Wang, W. Yang, Z. Chen, X. Zhong, S. P. Ringer, X. Liao, W. Liang and J. Huang, *Appl. Catal. B-Environ.,* 2021, **284**, 119759.
81 T. Xia, M. Ju, H. Qian, X. Bai, R. Lai, C. Xie, G. Yu, Y. Tang, C. Wang and Q. Hou, *J. Catal.*, 2024, **429**, 115257.
82 X. Xiao, Z. Ruan, Q. Li, L. Zhang, H. Meng, Q. Zhang, H. Bao, B. Jiang, J. Zhou, C. Guo, X. Wang and H. Fu, *Adv. Mater.*, 2022, **34**, 2200612.
83 J. Ding, Z. Teng, X. Su, K. Kato, Y. Liu, T. Xiao, W. Liu, L. Liu, Q. Zhang, X. Ren, J. Zhang, Z. Chen, O. Teruhisa, A. Yamakata, H. Yang, Y. Huang, B. Liu and Y. Zhai, *Chem*, 2023, **9**, 1017–1035.
84 Z. Xue, J. Yang, L. Ma, H. Li, L. Luo, K. Ji, Z. Li, X. Kong, M. Shao, L. Zheng, M. Xu and H. Duan, *ACS Catal.*, 2024, **14**, 249–261.
85 R. Sun, X. Cao, J. Ma, H.-C. Chen, C. Chen, Q. Peng and Y. Li, *Nat. Synth.*, 2025, **4**, 965–975.
86 S. Si, Y. Mao, Y.-A. Liu, J. Ma, W. Jiang, E.-D. Zhao, K. Song, H. Cheng, B. Huang, D. Liu and Y. Xiong, *Nat. Commun.*, 2025, **16**, 5128.
87 E.-R. Newmeyer, Y. Wang, Z. A. Long, J. D. North, Y. Shi and D. F. Swearer, *J. Am. Chem. Soc.*, 2025, **147**, 11789–11799.
88 L. Kang, B. Zhu, Q. Gu, X. Duan, L. Ying, G. Qi, J. Xu, L. Li, Y. Su, Y. Xing, Y. Wang, G. Li, R. Li, Y. Gao, B. Yang, X. Y. Liu, A. Wang and T. Zhang, *Nat. Chem.*, 2025, **17**, 890–896.
89 L. Xiong, H. Qi, S. Zhang, L. Zhang, X. Liu, A. Wang and J. Tang, *Adv. Mater.*, 2023, **35**, 2209646.
90 Y. Tao, J. Ding, Z. Teng, Q. Xu, W. Ou, H. Sun, S. Li, L. Yu, G. Li, B. Liu and C. Su, *J. Am. Chem. Soc.*, 2025, **147**, 18814–18825.
91 Y. Qin, P. Ren, J. Hu, S. Pradhan, T. H. Vuong, X. He, L. Alluhaibi, N. Rockstroh, S. Monti, G. Barcaro, A. Jaworski, P. Kuśtrowski, J. Rabeah, D. Hohenberger, S. Bagnich, A. Köhler, J. Breu, G. Vilé, M. Beller and S. Das, *Science*, 2026, **392**, eaed6068.
92 S. P, J. John, T. P. D. Rajan, G. M Anilkumar, T. Yamaguchi, S. C. Pillai and U. S. Hareesh, *J. Mater. Chem. A*, 2023, **11**, 8599–8646.
93 Z. Chen, A. G. Walsh and P. Zhang, *Acc. Chem. Res*., 2024, **57**, 521–532.
94 Z. Q. Chen, A. Ngan, C. Chan, J. Lee, D. D. Sanjaya and F. Gu, *Sol. PRL*, 2025, **9**, e2400804.
95 M. Agrachev, V. Giulimondi, I. Surin, S. Mitchell, G. Jeschke and J. Pérez-Ramírez, *Chem Catal*., 2024, **4**, 101136.
96 Y. Liu, X. Su, J. Ding, J. Zhou, Z. Liu, X. Wei, H. B. Yang and B. Liu, *Chem. Soc. Rev*., 2024, **53**, 11850–11887.
97 A. Hellmer, M. Molina-Torres and R. Mendoza-Cruz, *ACS Catal*., 2026, **16**, 10851–10881.
98 S.-M. Wu and P. Schmuki, *Adv. Mater*., 2025, **37**, 2414889.
99 L. Liu, T. Chen and Z. Chen, *Adv. Sci*., 2024, **11**, 2308046.
100 M. A. Hoque and M. I. Guzman, *Materials*, 2018, **11**, 1990.
101 M. Melchionna and P. Fornasiero, *ACS Catal*., 2020, **10**, 5493–5501.
102 R. A. Sheldon, *ACS Sustainable Chem. Eng*., 2018, **6**, 32–48.
103 A. Y. Chan, I. B. Perry, N. B. Bissonnette, B. F. Buksh, G. A. Edwards, L. I. Frye, O. L. Garry, M. N. Lavagnino, B. X. Li, Y. Liang, E. Mao, A. Millet, J. V. Oakley, N. L. Reed, H. A. Sakai, C. P. Seath and D. W. C. MacMillan, *Chem. Rev.* 2022, **122**, 2, 1485–1542.
104 C. Jiang, Y. Wang, G. Sheng, Ya. Liu, X. Han, Z. Li, C. Cheng, X. Zhao, Y. Zhou, Q. Zhang, M. Shang, Y. Zhu, Y. Su and Y. Cui, *Nat. Catal*., 2026, **9**, 666–675.
105 G. L. Puma and P. L. Yue, *Ind. Eng. Chem. Res*., 1999, **38**, 3246–3254.
106 J. Luo, V. Ruta, I. S. Kwon, J. Albertazzi, N. Allasia, O. Nevskyi, V. Busini, D. Moscatelli and G. Vilé, *Adv. Funct. Mater*., 2024, **34**, 2404794.
107 G. Wang, J. Zhang, L. Zhong and Z. Tang, *Ceram. Int*., 2024, **50**, 38532–38541.

Green Chemistry Accepted Manuscript

This review does not report new experimental or computational data. All information discussed in this article is derived from previously published studies.

Green Chemistry Accepted Manuscript